



Deposited via The University of Leeds.

White Rose Research Online URL for this paper:

<https://eprints.whiterose.ac.uk/id/eprint/131568/>

Version: Accepted Version

Article:

Liu, J, Liu, H, Wang, W et al. (2018) First Results From the Ionospheric Extension of WACCM-X During the Deep Solar Minimum Year of 2008. *Journal of Geophysical Research: Space Physics*, 123 (2). pp. 1534-1553. ISSN: 2169-9380

<https://doi.org/10.1002/2017JA025010>

Reuse

Items deposited in White Rose Research Online are protected by copyright, with all rights reserved unless indicated otherwise. They may be downloaded and/or printed for private study, or other acts as permitted by national copyright laws. The publisher or other rights holders may allow further reproduction and re-use of the full text version. This is indicated by the licence information on the White Rose Research Online record for the item.

Takedown

If you consider content in White Rose Research Online to be in breach of UK law, please notify us by emailing eprints@whiterose.ac.uk including the URL of the record and the reason for the withdrawal request.

1 **First Results from the Ionospheric Extension of WACCM-X during the**
2 **Deep Solar Minimum Year of 2008**

3
4

5 Jing Liu¹, Hanli Liu¹, Wenbin Wang¹, Alan G. Burns¹, Qian Wu¹, Quan Gan², Stanley C.
6 Solomon¹, Daniel R. Marsh¹, Liying Qian¹, Gang Lu¹, Nicholas M. Pedatella¹, Joe M.
7 McInerney¹, James M. Russell III³, and William S. Schreiner⁴

8
9

10 *¹High Altitude Observatory, National Center for Atmospheric Research, Boulder,*
11 *Colorado, USA*

12 *²Department of Physics and Astronomy, Clemson University, Clemson, SC, USA*

13 *³Hampton University, Hampton, Virginia, USA*

14 *⁴COSMIC Program Office, University Corporation for Atmospheric Research, Boulder,*
15 *Colorado*

16
17

18

19 Corresponding author: Jing Liu (jingliu@ucar.edu)

20
21

22 **Short Title:** WACCM-X Simulated Ionosphere

23
24

25

26

27

28

29

30

31

32 **Abstract**

33 New ionosphere and electrodynamics modules have been incorporated in the
34 thermosphere and ionosphere eXtension of the Whole Atmosphere Community Climate
35 Model (WACCM-X), in order to self-consistently simulate the coupled atmosphere-
36 ionosphere system. The first specified dynamics WACCM-X v.2.0 results are compared
37 with several datasets, and with the Thermosphere-Ionosphere-Electrodynamics General
38 Circulation Model (TIE-GCM), during the deep solar minimum year. Comparisons with
39 Thermosphere Ionosphere Mesosphere Energetics and Dynamics satellite of temperature
40 and zonal wind in the lower thermosphere show that WACCM-X reproduces the seasonal
41 variability of tides remarkably well, including the migrating diurnal and semidiurnal
42 components, and the non-migrating diurnal eastward propagating zonal wavenumber 3
43 component. There is overall agreement between WACCM-X, TIE-GCM, and vertical
44 drifts observed by the Communication/Navigation Outage Forecast System (C/NOFS)
45 satellite over the magnetic equator, but apparent discrepancies also exist. Both model
46 results are dominated by diurnal variations while C/NOFS observed vertical plasma drifts
47 exhibit strong temporal variations. The climatological features of ionospheric peak
48 densities and heights (NmF_2 and hmF_2) from WACCM-X are in general agreement with
49 the results derived from Constellation Observing System for Meteorology, Ionosphere
50 and Climate (COSMIC) data, although the WACCM-X predicted NmF_2 values are
51 smaller, and the equatorial ionization anomaly crests are closer to the magnetic equator
52 compared to COSMIC and ionosonde observations. This may result from the excessive
53 mixing in the lower thermosphere due to the gravity wave parameterization. These data-
54 model comparisons demonstrate that WACCM-X can capture the dynamic behavior of
55 the coupled atmosphere and ionosphere in a climatological sense.

56
57
58
59
60
61
62

63 **1. Introduction**

64 Capturing lower atmosphere forcing effects on the upper atmosphere is critical for
65 predicting ionosphere and thermosphere states because of the intimate coupling between
66 the lower and upper atmospheres. An earlier approach was to couple different models
67 covering different domains [e.g., Liu and Roble, 2002; Hagan et al., 2007]. This produces
68 artificial interfaces or boundaries and introduces unrealistic physical processes. In recent
69 years, several whole atmosphere models have been developed that cover the whole
70 Earth's atmosphere domain. Miyoshi and Fujiwara [2003] constructed the General
71 Circulation Model (GCM), which extends from the ground to the exobase. Later, this
72 model was updated to the coupled Ground-to-topside model of Atmosphere and
73 Ionosphere for Aeronomy (GAIA), including the neutral atmosphere from the
74 troposphere to the thermosphere, thermosphere-ionosphere coupling, and
75 electrodynamics [Jin et al., 2011]. The Whole Atmosphere Model (WAM) [Akmaev et al.,
76 2008; Fuller-Rowell et al., 2008], currently under development, is based on the National
77 Weather Service operational Global Forecast System model covering altitudes from the
78 ground to ~ 600 km. A thermosphere extension of the Whole Atmosphere Community
79 Climate Model (WACCM-X) also began its development several years ago [Liu et al.,
80 2010].

81 The usage of a whole atmosphere model has the following advantages [Roble, 2000]:
82 (1) treatment of the lower atmosphere and the upper atmosphere as a completely coupled
83 system in terms of physics, dynamics, and chemistry; (2) clarification of the possible
84 two-way interactions between climate change in the upper atmosphere and lower
85 atmosphere variability; (3) description of the climate response due to solar variability,
86 possibly through changes in middle and upper atmosphere chemistry and dynamics; (4) a
87 more accurate specification of shorter timescale changes in the thermosphere and
88 ionosphere. A comprehensive review of the whole atmosphere modeling efforts was
89 given by Akmaev [2011].

90 The ionosphere exhibits salient day-to-day variability due to lower atmosphere forcing,
91 geomagnetic forcing, and solar radiation changes. During geomagnetically quiet periods,
92 ionospheric day-to-day variability can be significantly impacted by lower atmospheric
93 forcing, especially by the variability of atmospheric waves [e.g. Forbes et al., 1993;

94 Lastovicka, 2006; Kazimirovsky and Vergasova, 2009; Liu, 2016 and references therein].
95 Tides can be generated in different altitudinal regions due to the following processes:
96 tropospheric latent heating, absorption of tropospheric infrared radiation by water vapor,
97 absorption of solar ultraviolet radiation by stratospheric ozone, thermosphere molecular
98 oxygen absorption of extreme ultraviolet radiation, and wave-wave interactions
99 [Chapman and Lindzen 1970; Hagan and Forbes, 2002; Liu, 2016]. There are two schools
100 of thoughts regarding the modulation of the ionosphere by tides: direct propagation of
101 atmospheric tides into the ionosphere and thermosphere [e.g., Oberheide et al., 2009] and
102 indirect coupling via the ionosphere E-region dynamo [e.g., Jin et al., 2008; Ren et al.,
103 2010; Wan et al., 2012]. The former denotes direct penetration of certain tidal modes
104 from the troposphere to the thermosphere, serving as an *in situ* source [Hagan et al.,
105 2007]. The latter refers to the tides producing variations in the E-region winds, which
106 modify the E-region dynamo. For instance, longitudinal variations of latent heating in the
107 troposphere can excite non-migrating tides in the lower atmosphere, which can propagate
108 upward and modify the wind in the MLT region [e.g., Immel et al., 2006; Wan et al.,
109 2012]. The winds in the lower thermosphere cause the E-region polarization electric
110 fields due to the differential motion between the ions and electrons. E-region dynamo
111 electric fields then map along magnetic field lines into the ionosphere F-region
112 ionosphere. Daytime eastward electric fields have great impacts on the latitudinal
113 distribution of low-latitude ionospheric electron density by modifying the F-region
114 ionospheric “fountain” effect.

115 Aside the aforementioned ionospheric dynamic effects, thermospheric composition and
116 thus ionospheric electron density can also be affected by lower atmospheric wave forcing
117 [e.g., Yue and Wang, 2014]. Seasonal variability of lower atmosphere tides is thought to
118 be one of the potential causes of similar ionosphere variations. Tides can modify the
119 upward propagation of gravity waves and their momentum deposition in the MLT region.
120 Gravity wave breaking, having a strong seasonal dependence, changes the eddy diffusion
121 in the lower thermosphere. This eddy diffusion has a tendency to transport O from the
122 lower thermosphere downward and molecular species upward, leading to a composition
123 change in the lower thermosphere. This effect is transmitted to higher altitudes through
124 molecular diffusion and vertical advection of neutral species in the thermosphere [e.g.,

125 Akmaev and Shved, 1980; Forbes et al., 1993; Qian et al., 2009; Yamazaki et al., 2013;
126 Yue and Wang, 2014; Burns et al., 2015]. Therefore, stronger eddy diffusion reduces the
127 thermospheric O/N₂ ratio and ionospheric F-region electron densities, as these two
128 parameters are positively correlated near the ionospheric F₂ peak height.

129 Most recently, ionospheric and electrodynamic modules have been incorporated in
130 WACCM-X, allowing us to self-consistently simulate the whole atmosphere from the
131 troposphere to the topside ionosphere without introducing any artificial interfaces
132 between the different layers of the atmosphere. The objective of this paper is to evaluate
133 this model by examining the first simulation results of this new version of WACCM-X
134 through comparisons of the modeled electron density, vertical ion drifts, and tidal
135 variability with multiple data sources, as well as with the Thermosphere-Ionosphere-
136 Electroynamics General Circulation Model (TIE-GCM) simulation results. These
137 comparisons have been performed for the deep solar minimum year 2008 when the
138 upward propagating lower atmospheric waves were expected to have stronger influences
139 on the upper atmosphere. A description of the numerical models and data used for this
140 study are given in the next section. Model-data comparisons are described in section 3.
141 Section 4 discusses the relevance of these results as related to observations. Conclusions
142 are given in section 5.

143

144 **2. Model and Data Descriptions**

145 **2.1 WACCM-X Introduction**

146 A detailed description of the new version (version 2.0) of WACCM-X (referred to as
147 WACCM-X v.2.0) can be found in Liu et al. [2018]. A brief summary is given here:
148 WACCM-X is an atmospheric component of the National Center for Atmospheric
149 Research (NCAR) Community Earth System Model (CESM), which couples atmosphere,
150 ocean, land surface, sea and land ice, and carbon cycle components through exchanging
151 fluxes and state information [Hurrell et al., 2013]. It is based on the community
152 atmosphere model (CAM) and Whole Atmosphere Community Climate Model
153 (WACCM). The first version of WACCM-X was described by Liu et al. [2010]. Key
154 developments and improvements of thermosphere and ionosphere modules in WACCM-
155 X v.2.0 include:

- 156 1. Improvements of the momentum equation and energy equation solvers to
157 account for the species dependence of atmosphere mean mass and specific
158 heats.
- 159 2. A new divergence-damping scheme that reduces unrealistic damping of
160 atmospheric tides.
- 161 3. Cooling by O(³P) fine structure emission.
- 162 4. A self-consistent electrodynamics module that solves the ionospheric electric
163 potential driven by the neutral wind dynamo.
- 164 5. A module that solves the transport of O⁺ in the F-region.
- 165 6. A time-dependent solver for electron and ion temperatures, and together with
166 thermospheric heating due to thermal electrons.
- 167 7. Metastable O⁺ chemistry and energetics.
- 168 8. Solar EUV ionization and heating that can accommodate solar spectra from
169 high-time-resolution models or measurements.
- 170 9. Specification of auroral inputs.

171 The top boundary of WACCM-X v.2.0 is set at 4.0×10^{-10} hPa (~500 to ~700km altitude,
172 depending on solar activity). The vertical resolution in the mesosphere and thermosphere
173 is a quarter of a scale-height, and the horizontal resolution is $1.9^\circ \times 2.5^\circ$ in latitude and
174 longitude, respectively. WACCM-X has the option to have the tropospheric and
175 stratospheric dynamics constrained to meteorological reanalysis fields for specifically
176 targeted time periods. All WACCM-X results used in the paper are from a specified
177 dynamics simulation of WACCMX, which is constrained up to 50 km by nudging
178 towards the National Aeronautics and Space Administration (NASA) Modern-Era
179 Retrospective Analysis for Research and Applications [Rienecker et al., 2011].

180

181 **2.2 TIE-GCM v.2.0**

182 The TIE-GCM is a community model developed at the NCAR High Altitude
183 Observatory. It is a first-principles, upper atmosphere, general circulation model that
184 solves the Eulerian continuity, momentum, and energy equations for the coupled
185 thermosphere/ionosphere system, covering the altitude range from approximately 97 km
186 to 600 km and having a horizontal resolution of $2.5^\circ \times 2.5^\circ$ and a vertical resolution of

187 1/4 pressure scale height [Roble et al., 1988; Richmond et al. 1992; Qian et al., 2012].
188 The main external drivers of the TIE-GCM are solar irradiance in the extreme-ultraviolet
189 and far-ultraviolet spectral regions, geomagnetic activity forcing including auroral
190 particle precipitation and ionospheric convection, and perturbation at the lower boundary
191 of the model by tides/waves. The tidal forcing at the height of the lower boundary (~97
192 km) is specified by GSWM diurnal and semidiurnal migrating and non-migrating tidal
193 amplitudes and phases [Hagan and Forbes, 2003].

194 TIE-GCM v.2.0 includes the following new physical features [Qian et al., 2014; Maute,
195 2017]: 2.5° horizontal resolution is supported; electrodynamic calculations are
196 parallelized; helium is calculated as a major species [Sutton et al., 2015]; argon is
197 calculated as a minor species; the geomagnetic field is updated to the International
198 Geomagnetic Reference Field version 12, and its annual secular variation is included for
199 the years 1900-2020.

200

201 **2.3 COSMIC Electron Density**

202 The Constellation Observing System for Meteorology Ionosphere and Climate
203 (COSMIC)/Formosat Satellite 3, a joint US/Taiwan radio occultation mission consisting
204 of six identical micro-satellites, were launched on 15 April 2006, and have provided more
205 than 4.4 million GPS radio occultation profiles to date. The ionospheric electron density
206 maps presented in this paper are obtained from the radio occultation Abel inversion
207 [Schreiner et al., 1999]. The Abel retrievals can cause systematic errors below the F layer
208 in regions where horizontal electron density gradients are large but give a good
209 estimation of the electron density in and above the F region, as well as peak electron
210 density (NmF_2) and peak height (hmF_2) [e.g., Lei et al., 2007; Yue et al., 2010]. A
211 Chapman α function was used to fit the ionospheric electron density profile between 170
212 and 600 km to derive NmF_2 and hmF_2 [e.g., Liu et al., 2009].

213

214 **2.4 SABER Temperature and TIDI Winds**

215 The Sounding of the Atmosphere using Broadband Emission Radiometry (SABER)
216 instrument was launched onboard the Thermosphere Ionosphere Mesosphere Energetics
217 Dynamics (TIMED) satellite on December 7, 2001. SABER measures the kinetic

218 temperature from CO₂ emission within the altitude range of 20-120 km and extends from
219 about 53° latitude in one hemisphere to 83° in the other. This viewing geometry
220 alternates and has complete local time coverage every 60 days. Local Thermodynamic
221 Equilibrium (LTE) and non-LTE retrieval algorithms are used, respectively, at altitudes
222 below 70 km and in the upper MLT region [Mertens et al. 2004]. As mentioned by
223 Remsberg et al. (2008), the random error in temperature data is less than 2 K below 70
224 km, and the error increases with altitude from 1.8 K at 80 km to 6.7 K at 100 km.

225 The TIMED Doppler Interferometer (TIDI) instrument on board TIMED provides
226 global horizontal winds from 70-120 km with a vertical resolution of 2 km using a limb-
227 scan Fabry-Perot interferometer. TIDI zonal winds in the MLT region are derived from
228 Doppler shift measurements of green line emissions. NCAR-processed O₂(¹Σ)
229 atmospheric band (0–0) P9 line (763.51 nm) TIDI data (version 0307) with a new zero
230 wind implementation were used for the current analysis [Killeen et al., 2006; Wu et al.,
231 2008]. We performed a space-time series spectral analysis to the southern and northern
232 tracks from a 60-d window separately, to obtain tidal amplitudes and phases of migrating
233 and non-migrating tides.

234

235 **3. Results**

236 **3.1 Ionospheric hmF₂ and NmF₂ Comparisons**

237 Figure 1 shows the monthly median hmF₂ comparison between WACCM-X (left
238 column), COSMIC (middle column), and TIE-GCM (right column) at March Equinox.
239 The white dotted line denotes the dip equator. In general, the monthly median hmF₂
240 exhibits obvious diurnal variation and this diurnal variation has a clear latitudinal
241 dependence. For instance, at middle latitudes, ionospheric hmF₂ is higher during
242 nighttime than during daytime. Nighttime hmF₂ at middle latitudes is slightly
243 underestimated by WACCM-X. Over the dip equator, daytime eastward dynamo electric
244 fields produce upward ion drifts and are very effective at elevating the equatorial
245 ionosphere to higher altitudes. That is why hmF₂ peaks around the equator on the dayside.
246 This feature is well represented by WACCM-X and TIEGCM. Another noteworthy
247 feature is that the global pattern of hmF₂ has a clear UT/longitude dependence, arising
248 from the effects of, the offsets between geomagnetic and geographic poles, magnetic field

249 declination, and non-migrating tides [e.g., Immel et al., 2006; Wan et al., 2012; Zhang et
250 al., 2013; Liu et al., 2017].

251 Figure 2 is similar to Figure 1 but for June solstice. Apparently, daytime equatorial
252 hmF₂ peaks move northward a little bit compared to those at March Equinox. In addition,
253 nighttime middle latitude hmF₂ exhibits hemispheric asymmetry and hmF₂ in the summer
254 hemisphere is higher than that in the winter hemisphere. This feature is well captured by
255 WACCM-X and TIEGCM. This asymmetry is probably due to the mean summer-to-
256 winter neutral flow and temperature effects. Mean summer-to-winter winds push the
257 ionosphere upward in the upwind hemisphere (summer hemisphere) and press the
258 ionosphere downward in the downwind hemisphere (winter hemisphere). In addition,
259 stronger thermal expansion in the summer hemisphere also uplifts the ionosphere to
260 higher altitudes, augmenting this seasonal asymmetry.

261 Figure 3 illustrates the monthly median NmF₂ comparisons between WACCM-X (left
262 column), COSMIC (middle column), and TIE-GCM (right column) at March Equinox.
263 NmF₂ is well arranged in geomagnetic coordinates. The low latitude equatorial ionization
264 anomaly (EIA) is characterized by a minimum around the dip equator and two peaks
265 around $\pm 15^\circ$ geomagnetic latitudes. In general, WACCM-X daytime NmF₂ is smaller at
266 low latitudes than COSMIC and TIE-GCM. In addition, the two crests of the EIA from
267 WACCM-X are closer to the dip equator than those in COSMIC data and TIE-GCM. The
268 latitudinal separation of the two EIA peaks of both WACCM-X and COSMIC varies with
269 universal time. The largest latitude distances between the two EIA crests are 32°
270 (WACCM-X) and 39° (COSMIC) at 00 UT, 32° (WACCM-X) and 45° (COSMIC) at 06
271 UT, 26° (WACCM-X) and 29° (COSMIC) at 12 UT, and 32° (WACCM-X) and 39°
272 (COSMIC) at 18 UT.

273 Figure 4 is similar to Figure 3 with a different color scale but at June solstice.
274 Compared to NmF₂ at March equinox, there is an overall NmF₂ reduction at June solstice,
275 which is characteristic of the semi-annual variation in ionospheric electron density [e.g.,
276 Burns et al., 2012; Qian et al., 2013]. At most UTs (0000, 0600, 1200 UT), the COSMIC
277 data shows that the EIA crest in the winter hemisphere is stronger than that in the summer
278 hemisphere from morning to noon; however, from noon to early afternoon, the winter
279 EIA crest is weakened, and the crest in the summer hemisphere is intensified. Similar

280 EIA winter-summer asymmetry has been reported in the published literature and has been
281 explained by the relative contributions from electrodynamics, thermodynamics, and
282 chemical processes [e.g., Lin et al., 2007]. The simulated EIA features calculated by the
283 two models somewhat differ from the COSMIC observations. At 0000 UT (first panels),
284 for instance, COSMIC NmF₂ is weaker in the winter (south) crest than it in the summer
285 (north) one in the longitude range from -180° to -120°, whereas both WACCM-X and
286 TIE-GCM NmF₂ exhibit different characteristics, namely, the Southern EIA crest is
287 stronger than the Northern crest within the longitude range from -180° to -120°. At 0600
288 and 1200 UT, this transition is roughly captured by WACCM-X and TIE-GCM. At 1800
289 UT, COSMIC NmF₂ is generally stronger in the Northern EIA crest than the Southern
290 EIA crest, while WACCM-X simulated EIA crest is stronger in the South.

291 Detailed comparisons between WACCM-X and ionosonde observations are shown in
292 Figures 5 and 6. Figure 5 gives hourly ionosonde-observed (black line) and WACCM-X
293 (red line) (a) NmF₂ and (c) hmF₂ over Jicamarca (12°S, 283°W, 1°N geomagnetic
294 latitude) during days 300-320 in 2008. Scatter plots between hourly observations and
295 WACCM-X of (b) NmF₂ and (d) hmF₂ are for days 60-366 of year 2008. Both the model
296 and observations exhibit salient day-to-day variability. An obvious feature in Figure 5a is
297 the dramatic daytime NmF₂ enhancement around DOY 314. This could be related to the
298 effects of recurrent geomagnetic storms generated by solar wind high-speed streams [e.g.,
299 Liu et al., 2012]. WACCM-X can generally capture the NmF₂ variability, but tends to
300 underestimate the daytime NmF₂ by ~50%. Figure 5b also shows that the data are mostly
301 located in the lower part of the plot, indicating systemically lower modeled NmF₂ values.

302 Figure 5c shows that equatorial hmF₂ is highly variable during this period (days 300–
303 320) in both observations and model output. There is a reasonable agreement between
304 WACCM-X and the observations in magnitude. The dots in Figure 5d are evenly
305 distributed on both sides of the reference line. The highly variable hmF₂ over the equator
306 shows that the electrodynamics processes undergo significant variability, probably caused
307 by diurnal variations of lower atmospheric tide forcing, magnetospheric penetration
308 electric fields and disturbed dynamo electric fields in association with recurrent
309 geomagnetic storms [e.g., Liu et al., 2012]. The correlation coefficient is lower in Fig. 5d,
310 probably related to the offset in temporal variations between data and model, whereas in

311 Fig. 5c, both are dominated by the comparatively larger diurnal variation of NmF₂, so the
312 correlation is high.

313 Figure 6 is similar to Figure 5, but over Boulder (40.0° N, 254.7° W, 48.9°
314 geomagnetic latitude). Also, Figure 6a and 6c show ionosphere parameters during days
315 311–330 in 2008. This 11-day time shift between Figure 5 and Figure 6 is because there
316 is large data gap over Boulder during days 300–320 in 2008. A bias still exists in NmF₂
317 for the whole year with the modeled NmF₂ values being about half of the observed ones
318 in the daytime, as shown in Figure 6b. WACCM-X misses some spikes that are seen in
319 observed hmF₂ (figure 6c). On the one hand, this simulation is driven by the low-
320 resolution Kp index, which could miss prompt penetration electric fields effects or
321 travelling atmosphere disturbances (TAD). Under the effects of penetration electric fields
322 or TAD, the ionosphere can undergo dramatic elevation or depression depending on the
323 direction of electric fields or TAD. On the other hand, this discrepancy could also
324 represent problems with the spiky changes in hmF₂ observed by ionosondes during the
325 nighttime.

326 Electric-field-induced vertical drifts have great impacts on the low-latitude ionospheric
327 structure. Figure 7 compares the equatorial vertical drifts over Jicamarca with those from
328 WACCM-X at 300 km (red solid line), TIE-GCM at 300 km (red dashed line), the
329 Scherliess-Fejer (S-F) model (blue solid line), and the Communication/Navigation
330 Outage Forecast System (C/NOFS) satellite. The Scherliess-Fejer model and C/NOFS
331 vertical drift data were obtained from Stoneback et al. [2011]. Drifts from the Scherliess-
332 Fejer model are based largely on Jicamarca radar and satellite datasets [Scherliess and
333 Fejer, 1999]. C/NOFS data during the years of 2008–2009 within ±5° magnetic latitudes
334 and in the longitude range of 240°–300° E are binned according to season. In general,
335 vertical drifts from these models are dominated by diurnal variations, whereas
336 observations are characterized by strong temporal variations depending on the season.
337 The three models (WACCM-X, TIE-GCM, and S-F model) exhibit similar features, with
338 strong upward vertical drifts at local noon and weak or downward drifts in the evening.
339 Large discrepancies still exist between these three models and C/NOFS. For example,
340 WACCM-X tends to overestimate the downward drifts at around midnight for all four

341 seasons. In March equinox, the three models fail to capture the C/NOFS observed
342 downward drifts at around 1500 LT.

343 At March Equinox, this comparison highlights the presence of semi-diurnal or
344 terdiurnal components of measured ion drifts, characterized by upward drifts in the post-
345 midnight (0200-0400 LT), daytime (0800-1400 LT), and early night (1800-2300 LT).
346 The postmidnight upward equatorial drifts may be related to thermospheric dynamics in
347 association with the midnight temperature maximum [Stoneback et al., 2011; Fang et al.,
348 2016]. There is an overall agreement between models and observations in capturing
349 daytime upward drifts. However, all three models tend to underestimate the early night
350 upward drifts and fail to capture the strong downward drifts with a magnitude of 50 m/s
351 at around 0600 LT.

352 At June Solstice, the observed vertical drifts exhibit similar variations to those at the
353 March equinox, but they are shifted to later local times by about 2 hours. The three
354 models overestimated daytime drifts. Inconsistencies also exist in the post-midnight
355 sector in which models predict downward drifts with a magnitude of 10 m/s, whereas the
356 C/NOFS data show upward drifts.

357 At September Equinox, C/NOFS observed vertical drifts are less than 10 m/s and
358 smaller than those of the 3 models. WACCM-X overestimates the downward drift in the
359 post-midnight sector by about 10 m/s relative to the S-F model and TIE-GCM.

360 At December Solstice, C/NOFS observed vertical drifts are characterized by semi-
361 diurnal variations and are upward at around 1000–1400 LT and 2000–0400 LT. The late
362 morning and afternoon upward vertical drifts are prominent and well captured by models.
363 The models, however, failed to reproduce the upward drifts in the nighttime sector
364 (2000–0400 LT).

365

366 **3.2 Tidal Comparisons**

367 Tides play important roles in modulating the neutral wind dynamo in the lower
368 thermosphere and the E-region ionosphere. The WACCM-X-simulated, migrating,
369 diurnal, zonal wavenumber 1 (DW1, Figure 8) and semi-diurnal, zonal wavenumber 2
370 (SW2, Figure 9) tides, and non-migrating, eastward-propagating, diurnal tide with zonal
371 wavenumber 3 (DE3, Figure 10) are compared with the TIMED satellite observations for

372 2008 in this section. Figure 8 compares the temperature (upper panels) and zonal wind
373 (bottom panels) amplitudes of DW1 between WACCM-X (left columns) and
374 observations (right columns) at March Equinox, when DW1 maximizes [e.g., Zhang et al.,
375 2006; Gan et al., 2014]. Overall, for DW1, there is a good agreement between the
376 WACCM-X simulations and TIMED measurements of zonal winds and temperatures in
377 terms of spatial structure, with the primary peak located at the equator and between 95-
378 105 km. The DW1 temperature amplitude from WACCM-X reaches 17.5–20 K, which is
379 ~3–5 K lower than the DW1 amplitude from SABER data, though it agrees with the
380 DW1 amplitude obtained from 2002-2006 SABER analysis [Akmaev et al., 2008]. The
381 secondary peaks of ~10 K occur at around $\pm 40^\circ$ S/N within the altitude range of 95–110
382 km for both WACCM-X and SABER. The DW1 zonal wind amplitude from WACCM-X
383 has a similar spatial pattern to the TIDI DW1 zonal wind amplitude, with a maximum at
384 around $\pm 30^\circ$ and a larger amplitude in the southern hemisphere. The wave amplitude
385 from WACCM-X, however, is weaker than that found in the TIDI analysis, with the
386 WACCM-X peak amplitude in the southern hemisphere being ~30 m/s less than that
387 from the TIDI data.

388 Figure 9 shows height versus geographic latitude distributions of the migrating
389 semidiurnal tide (SW2) temperature and zonal wind amplitudes in July, when SW2
390 attains its largest magnitude. The temperature amplitude maxima from WACCM-X are
391 located at latitudes near 30° and altitudes of ~115 km in the NH and near -15° at above
392 120 km in the SH. The summer hemisphere maximum (~50 K) is stronger than the winter
393 one (~30 K), and the summer hemispheric amplitude at 110 km is slightly larger than that
394 in the SABER data. The zonal wind amplitude maximizes at higher geographic latitudes
395 (~ 50°) and has the same summer-winter seasonal dependence. The peak summer
396 hemispheric amplitude from the model (~55m/s) is weaker than that from the TIDI data
397 (larger than 60m/s).

398 Figure 10 illustrates the cross-section of DE3 temperature and zonal wind amplitudes
399 in July. There is also a general agreement in the spatial structures between WACCM-X
400 and the TIMED data. The latitudinal structure of the DE3 tide above 100 km height is
401 approximately symmetrical about 10° S, but some contribution of the asymmetric DE3
402 tidal modes has been found below 95 km as well. SABER temperature amplitude tends to

403 maximize at 105–118 km with amplitudes of 15–20 K, whereas DE3 in zonal winds
404 attain their largest values at somewhat lower altitudes compared with those of the
405 temperature. The peak DE3 temperature amplitude from WACCM-X is 8–10 K, weaker
406 than the SABER analysis for 2008, although the DE3 amplitude agrees with the SABER
407 DE3 analysis over 2002–2006 (at 116 km, Akmaev et al., 2008). The peak DE3 zonal
408 wind amplitude from WACCM-X is ~10 m/s less than that from the TIDI DE3 analysis.

409 Figure 11 shows the seasonal variation of temperature amplitudes in DW1 (upper
410 panel), DE3 (middle panel), and SW2 (lower panel) at 95, 110, and 105 km, respectively,
411 for both WACCM-X (left column) and SABER (right column). Both WACCM-X and
412 SABER show the distinctive signature of the first symmetric propagating component of
413 DW1, namely a maximum at the equator and secondary maxima near $\pm 35^\circ$ latitudes. As
414 seen in previous plots, the DW1 amplitude in WACCM-X temperatures (9–15 K) is less
415 than that in SABER temperatures (15–18 K). The secondary peak from SABER is located
416 at around $\pm 35^\circ$ geographic latitude, where the tidal amplitude reaches 6–9 K. The top
417 panels indicate a strong semi-annual variation of DW1, with the maximum and minimum
418 amplitudes during the equinoxes and solstices, respectively, in WACCM-X and SABER
419 at 95 km. It is also evident that the maximum at the March equinox is larger than that at
420 the September equinox. The DW1 variation has been well recorded by ground-based and
421 satellite observations [e.g., McLandress et al., 1996; Zhang et al., 2006; Gan et al., 2014]
422 and explained by either similar variation of heating sources [Hagan and Forbes, 2002;
423 Lieberman et al., 2003], semi-annual variation of stratosphere and mesosphere
424 background winds [McLandress, 2002], or similar damping within the MLT region [Xu et
425 al., 2009; Lieberman et al., 2010].

426 The SABER DE3 temperature amplitude is dominated by an annual variation. The
427 SABER DE3 distribution is symmetric about 5°S latitude with maximum amplitudes
428 (~18 K) between July and October, and minimum amplitudes between December and
429 May. The WACCM-X amplitudes have a similar peak (~12 K) in September and
430 minimize at around November. However, WACCM-X predicts a secondary DE3 peak
431 around January, which is much weaker in SABER observations.

432 The SW2 tide shows a clear semi-annual variation with maxima around the solstices.
433 At the altitude examined here (105km), SABER SW2 has the strongest amplitude in

434 August and secondary peaks in December, and the northern and southern peaks are
435 comparable. WACCM-X SW2, on the other hand, has peaks in the summer hemisphere
436 and amplitudes at the two solstices are comparable. The temperature tide from WACCM-
437 X is stronger in the NH (~ 18 K) than in the SH (~ 12 K), but these values are weaker
438 than the temperature tidal amplitudes of the tides measured by SABER. It should be
439 noted that the SW2 tide and its seasonal variation might change quite rapidly with
440 altitude (and probably also inter-annually). For example, the SABER SW2 analysis for
441 the time period of 2002–2006 display larger peaks in the winter hemisphere, and the peak
442 values at the two solstices are comparable at 100 km [Akmaev et al., 2008]. Similar
443 latitudinal/seasonal dependence is also seen in the SW2 zonal and meridional wind
444 amplitudes at ~95 km in WACCM-X [Liu et al., 2018].

445 Seasonal variations of lower and middle atmosphere processes can modify
446 thermospheric composition and electrodynamics, and thus contribute to the ionospheric
447 seasonal variability. As shown in Figure 12, seasonal variations of the ionosphere are
448 prominent both in the model and observations from the COSMIC satellites. The median
449 of these NmF₂ values was calculated for all local solar times between 0900 and 1500 for
450 all longitudes and 3-degree bins in magnetic latitude. Several noticeable features in the
451 mid- and low-latitude ionosphere are seen in this plot. The most salient feature is that
452 COSMIC NmF₂ has two peaks around equinoxes and exhibits equinoctial asymmetry
453 with larger values at March Equinox. The WACCM-X NmF₂ has a similar semiannual
454 variation even though WACCM-X tends to underestimate the NmF₂ at mid- and low-
455 latitudes.

456 WACCM-X simulated hmF₂ is in reasonable agreement with that from COSMIC.
457 Both COSMIC observations and WACCM-X simulations indicate that hmF₂ tends to
458 maximize around the magnetic equator and has a preference for the summer side due to
459 the effects of neutral winds and temperature [Rishbeth, 1998]. The discrepancy lies in
460 that WACCM-X simulated hmF₂ is about 20–50 km higher in the equatorial regions of
461 both hemispheres and about 20 km lower in the middle latitudes of the northern
462 hemisphere.

463

464 **4. Discussion**

465 Comprehensive comparisons between WACCM-X and several datasets indicate that
466 WACCM-X is able to capture realistic tides and ionospheric features. Quantitatively,
467 however, apparent discrepancies between model results and observations also exist,
468 indicating the need for further improvement of the model.

469 **4.1 Equatorial Ionization Anomaly Model-Data Comparisons**

470 One of the model-data discrepancies concerns the fact that the WACCM-X simulated
471 EIA is weaker and closer to the equator than the EIA seen in COSMIC observations. It is
472 well established that electric fields play important roles in shaping the EIA structure
473 [Rishebeth, 2000]. In the presence of a near horizontal magnetic field, the EIA is formed
474 by the eastward daytime electric field pushing plasma upward; this in turn affects
475 ambipolar diffusion along field lines. The detailed comparison in Figure 7 illustrates that
476 downward ion drifts from WACCM-X in the post-midnight sector are much stronger than
477 those in the TIE-GCM and the S-F empirical model, as well as C/NOFS observations.
478 Downward ion drifts reduce the electron density due to fast chemical reactions in the
479 thermosphere-ionosphere system below the F₂ peak. The E-region dynamo is driven by
480 poleward neutral winds in the thermosphere [see *Heelis*, 2004 and references therein].
481 Any process that can modulate either the winds or the electric fields that they create can
482 modify the strength of the EIA. The tidal winds in the E-region ionosphere modulate the
483 EIA through the E-region dynamo. This requires a more realistic tidal specification in the
484 ionosphere electric dynamo region. It is anticipated that assimilating the lower
485 atmosphere data into WACCM-X will capture more realistic tidal features [e.g., Pedatella
486 et al., 2013].

487 Apart from electric fields, stronger ambipolar diffusion, lower O/N₂, and
488 thermosphere winds could also be responsible for the overall reduction in WACCM-X
489 simulated NmF₂ in the EIA region. Low O/N₂ in the thermosphere could be related to
490 strong tidal or gravity wave dissipation in WACCM-X, leading to stronger eddy diffusion
491 around the mesopause. A plausible cause of this discrepancy is then that the eddy
492 diffusion from the current gravity wave parameterization scheme used in the model is too
493 large and continues to grow with altitude till ~200 km. This eddy diffusion can transport
494 O from the lower thermosphere downward and molecular species (N₂) upward, leading to
495 a compositional change in the lower thermosphere. This effect will be transmitted to

496 higher altitudes by vertical advection and molecular diffusion of neutral species in the
497 thermosphere. Generally, because of a larger scale height of O than N₂, stronger eddy
498 diffusion increases mixing and thus reduces the O/N₂ ratio [Forbes et al., 1993;
499 Lastovicka, 2006; Kazimirovsky and Vergasova, 2009; Qian et al., 2009]. The O/N₂ ratio
500 is positively correlated with electron density through production by solar EUV radiation
501 and loss through recombination with the molecular neutral species. Sensitivity tests (not
502 shown here) illustrate that turning off the eddy diffusion above the turbopause increases F
503 region ionospheric electric density.

504

505 **4.2 WACCM-X Simulated Seasonal Variations of Ionospheric NmF₂ and hmF₂**

506 Figure 12 compares the daytime climatology of NmF₂ and hmF₂ observed by
507 COSMIC and simulated by WACCM-X. COSMIC hmF₂ is generally dominated by an
508 annual variation that peaks on the summer side of the magnetic equator. This is
509 associated with the prevailing summer-to-winter mean flow (Figure 12), which raises the
510 ionosphere in the upwind (summer) hemisphere and lowers the ionosphere in the
511 downwind (winter) hemisphere. This prevailing summer-to-winter mean flow also drives
512 an annual variation on O/N₂ and NmF₂ (Figure 12) at midlatitudes.

513 Daytime, low-latitude, ionospheric NmF₂ exhibits annual and semiannual variations,
514 with maxima near equinoxes, a primary minimum at June solstice, and a secondary
515 minimum in December solstice. These general features are captured by WACCM-X.
516 Differences also occur. The model simulated NmF₂ semiannual variation is weaker than
517 that measured by COSMIC. Another noticeable difference between WACCM-X results
518 and COSMIC observations is that the model-simulated, seasonal peak of the northern
519 EIA crest extends into January, whereas the observed one is confined near March. There
520 is an offset in the month of the peak between the model and the data at September
521 equinox maxima: in the observations the northern hemisphere peak occurs near October
522 and the southern hemisphere one after October, whereas in the model simulations the
523 northern hemispheric peak is offset towards the winter solstice but the southern one,
524 which is much weaker, occurs near September.

525 There is no agreement yet on the cause of the semiannual variations of NmF₂,
526 although it is clearly related to the semiannual variation in thermospheric composition.

527 Several mechanisms have been proposed to explain this phenomenon, including
528 competing effects between O/N₂ changes caused by thermosphere circulation and solar
529 zenith angle [e.g., Millward et al., 1996; Rishbeth, 1998], a more mixed thermosphere in
530 solstice than in equinox caused by global-scale inter-hemispheric thermosphere
531 circulation [e.g., Fuller-Rowell, 1998], eddy diffusion by gravity wave dissipation [e.g.,
532 Qian et al., 2009; 2013], and semi-annual variations of geomagnetic forcing [Cliver et al.,
533 2000 and references therein].

534 It is worth mentioning that O/N₂ exhibits semiannual variations that maximize at the
535 equinoxes and minimize at the solstices in the equatorial region (Figure 12). However,
536 the peak-to-valley ratio of the semiannual components in WACCM-X O/N₂ over the
537 magnetic equator is much weaker than that found by Qian et al., [2009] after adjusting
538 the seasonal variation of eddy diffusion at the lower boundary of the TIE-GCM. The
539 weak semi-annual variations in the simulated O/N₂ can lead to weaker seasonal variations
540 in low-latitude NmF₂. This O/N₂ semiannual variation is mostly related to thermosphere
541 circulation effects, which are caused by internal thermospheric dynamics [Fuller-Rowell,
542 1998] and mesosphere eddy diffusion [Qian et al., 2009]. Improper parameterization of
543 seasonal variations of eddy diffusion caused by gravity waves could be one potential
544 cause. The eddy diffusion coefficient K_{zz} is a product of the gravity wave
545 parameterization in the model [Garcia et al., 2007; Richter et al. 2010]. In WACCM-X,
546 the low-latitude K_{zz} value at 110 km peaks from May to October as shown in Figure 12.
547 Increasing K_{zz} reduces the O/N₂ ratio and depletes electron density. Qian et al. [2013]
548 compared the TIE-GCM runs with and without the seasonal variations of eddy diffusion
549 at the lower boundary and showed that imposing seasonally variable eddy diffusion
550 improves the comparison between the modeled and COSMIC-observed NmF₂. It should
551 be noted that K_{zz} in WACCM-X represents the effects of sub-grid turbulent mixing. It is
552 different from the TIE-GCM K_{zz}, which represents not only all sub-grid mixing
553 processes that are not captured by the model, regardless of causes, but also the effects
554 from all other lower and middle atmospheric processes that produce variability in vertical
555 transport at and above the mesopause region where the model lower boundary is located
556 [Qian et al., 2013; Qian et al., 2017]. Very limited observations related to eddy diffusion
557 are available: those that are show that eddy diffusion is larger during the solstices than

558 during the equinoxes, with stronger turbulence in summer than in winter [e.g., Kirchhoff
559 and Clemesha, 1983; Fukao et al., 1994; Sasi and Vijayan, 2001]. This could be one of
560 the potential causes of the discrepancy.

561 An additional source of the discrepancy between modeled and observed NmF₂ is the
562 very weak seasonal variation of the modeled vertical drifts, as illustrated in Figure 12.
563 Equatorial vertical drifts maximize at March equinox, with a magnitude of about 20 m/s
564 and are similar in other months. However, previous studies demonstrated that equatorial
565 vertical drifts exhibit a strong seasonal variation [e.g., Fejer et al., 2008; Su et al., 2008;
566 Kil et al., 2009]. As shown in Figure 7 in Kil et al. [2009], the observed daytime vertical
567 drifts show a strong semiannual variation, peaking at the equinoxes with magnitudes of
568 ~22 m/s. The modeled vertical drifts are closer to the observed ones at March equinox,
569 but are weaker than those at September Equinox. Lack of a semiannual variation in the
570 vertical drifts modifies the seasonal variation of the daytime “fountain” effect, and thus
571 modifies the seasonal variation of electron density correspondingly. This could be one of
572 the potential causes of the discrepancy between WACCM-X and the data regarding the
573 low latitude seasonal variation of NmF₂. But it is unclear to what degree such a weak
574 semi-annual variation in vertical drifts can be responsible for the rather large difference
575 in the seasonal variation of NmF₂ between the model and the observations.

576 Several possible mechanisms have been proposed to explain the semiannual variation,
577 and there could be complex interactions among these processes. Further investigation is
578 thus needed in future studies to explore the relative contribution of the above-mentioned
579 processes, as well as other processes.

580

581 **5. Conclusions**

582 The first ground-to-space simulation results from WACCM-X with a self-consistent
583 ionosphere and electrodynamics reveal a realistic representation of the seasonal variation
584 of migrating and non-migrating tides, ionospheric electric fields induced vertical ion
585 drifts, NmF₂, and hmF₂. Comparisons with observations from the TIMED satellite in the
586 lower thermosphere show that WACCM-X reproduces the seasonal variability of tides
587 remarkably well, including DW1, DE3, and SW2. Comparisons between WACCM-X and
588 COSMIC ionospheric parameters show that WACCM-X can capture the ionosphere

589 morphology during the deep solar minimum year of 2008 reasonably well. However, it
590 should be noted that there is considerable evidence that the F-region ionosphere was, on
591 average, as much as 10% lower in density during 2008–2009 than during previous solar
592 minima, and that solar EUV radiation parameterized using the $F_{10.7}$ index cannot fully
593 account for this effect [Solomon et al., 2013]. The WACCM-X and TIE-GCM runs
594 performed for this study employed $F_{10.7}$ without any adjustment, so they should be
595 expected to be slightly higher than COSMIC observations; instead of they are somewhat
596 lower. Nevertheless, the detailed model-data comparisons have revealed the following
597 main findings:

598 1. There is an overall agreement between model and data in the tides and the diurnal
599 variations of ionospheric parameters (hmF_2 and NmF_2). The EIA crest is stronger in the
600 winter hemisphere in the morning sector and gives way to the summer hemisphere in the
601 afternoon sector. In spite of the general agreement of the spatial structures of NmF_2 , the
602 model NmF_2 is often lower than observations. At some locations, WACCM-X simulated
603 NmF_2 is almost half of the observation. hmF_2 is higher over the equator in the daytime
604 and pre-midnight sector, whereas it is higher at middle latitudes in the post-midnight
605 sector. Daytime upward ion drifts are seen in WACCM-X, TIE-GCM, and C/NOFS, but
606 there are differences among them. For instance, model results (WACCM-X and TIE-
607 GCM) are dominated by diurnal variations, whereas observations have more temporal
608 variability over equator.

609 2. Complicated seasonal variations are seen in ionospheric NmF_2 , hmF_2 , and tidal
610 components at middle and low latitudes in the deep solar minimum year of 2008. During
611 daytime, equinoctial asymmetry and semiannual variations are present in both WACCM-
612 X and COSMIC NmF_2 . WACCM-X captures the peak of the DE3 temperature tide at
613 June solstice well, whereas the additional peak of the DE3 temperature tide at the
614 December Solstice is only seen in WACCM-X, but not in the SABER observations.
615 There is a good consistency between WACCM-X and SABER SW2 temperature tidal
616 components in terms of seasonal variations. Both of them maximize at the June solstice,
617 with a secondary peak around the December solstice.

618 These comparisons give us confidence that WACCM-X can be a useful tool in
619 studying the complex dynamics, electrodynamics, and chemical processes in the whole
620 atmosphere system.

621

622 **Acknowledgements**

623 We acknowledge the CESM, CAM, WACCM, and WACCM-X development teams at
624 NCAR and, in particular, Art Richmond, Ben Foster, and Francis Vitt for key
625 contributions to WACCM-X. We would like to also acknowledge NASA grants NASA
626 grants NNX13AE20G, NNX14AE06G, NNX14AF20G, NNX14AH54G, and
627 NNX15AB83, and NSF grant 1135432, and AFOSR grant FA9550-16-1-0050. The TIDI
628 and SABER datasets are obtained from <http://timed.hao.ucar.edu/tidi/data.html> and
629 <http://saber.gats-inc.com/>, respectively. COSMIC electron density is available at
630 <http://cdaac-www.cosmic.ucar.edu/cdaac/products.html>. WACCM-X and TIE-GCM are
631 open-source community models; output from model runs used in this study are archived
632 on the NCAR High Performance Storage System. NCAR is sponsored by the National
633 Science Foundation.

634

635 **References**

- 636 Akmaev, R. A., and G. M. Shved (1980), Modelling of the composition of the lower
637 thermosphere taking account of the dynamics with applications to tidal variations
638 of the forbidden O I 5577 Å airglow, *Journal of Atmospheric and Terrestrial*
639 *Physics*, 42, 705–716.
- 640 Akmaev, R. A., T. J. Fuller-Rowell, F. Wu, J. M. Forbes, X. Zhang, A. F. Anghel, M. D.
641 Iredell, S. Moorthi, and H.-M. Juang (2008), Tidal variability in the lower
642 thermosphere: Comparison of Whole Atmosphere Model (WAM) simulations with
643 observations from TIMED, *Geophys. Res. Lett.*, 35, L03810,
644 doi:10.1029/2007GL032584.
- 645 Akmaev, R. A. (2011), Whole atmosphere modeling: Connecting terrestrial and space
646 weather, *Rev. Geophys.*, 49, *RG4004*, doi:10.1029/2011RG000364.
- 647 Burns, A. G., S. C. Solomon, W. Wang, L. Qian, Y. Zhang, and L. J. Paxton (2012),
648 Daytime climatology of ionospheric NmF2 and hmF2 from COSMIC data, *J.*
649 *Geophys. Res.*, 117, A09315, doi: 10.1029/2012JA017529.
- 650 Chapman, S., and R. S. Lindzen (1970), *Atmospheric Tides: Thermal and Gravitational*,
651 200 pp., Gordon and Breach, New York.
- 652 Cliver, E. W., Y. Kamide, and A. G. Ling (2000), Mountains versus valleys: Semiannual
653 variation of geomagnetic activity, *J. Geophys. Res.*, 105(A2), 2413–2424,
654 doi:10.1029/1999JA900439.

655 Dickinson, R. E., E. C. Ridley, and R. G. Roble (1981), A three dimensional general
656 circulation model of the thermosphere, *J. Geophys. Res.*, 86, 1499–1512.

657 Fang, T.-W., R. A. Akmaev, R. A. Stoneback, T. Fuller-Rowell, H. Wang, and F. Wu
658 (2016), Impact of midnight thermosphere dynamics on the equatorial ionospheric
659 vertical drifts, *J. Geophys. Res. Space Physics*, 121, 4858–4868,
660 *doi:10.1002/2015JA022282*.

661 Fejer, B. G., J. W. Jensen, and S.-Y. Su (2008), Quiet time equatorial F region vertical
662 plasma drift model derived from ROCSAT-1 observations, *J. Geophys. Res.*, 113,
663 A05304, *doi: 10.1029/2007JA012801*.

664 Forbes, J. M., R. G. Roble, and C. G. Fesen (1993), Acceleration, heating, and
665 compositional mixing of the thermosphere due to upward propagating tides,
666 *Journal of Geophysical Research: Space Physics*, 98(A1), 311–321,
667 *doi:10.1029/92JA00442*.

668 Fukao, S., M. D. Yamanaka, N. Ao, W. K. Hocking, T. Sato, M. Yamamoto, T.
669 Nakamura, T. Tsuda, and S. Kato (1994), Seasonal variability of vertical eddy
670 diffusivity in the middle atmosphere: 1. Three-year observations by the middle
671 and upper atmosphere radar, *J. Geophys. Res.*, 99, 18,973–18,987.

672 Fuller-Rowell, T. J. (1998), The “thermospheric spoon”: A mechanism for the
673 semiannual density variation, *J. Geophys. Res.*, 103, 3951–3956.

674 Fuller-Rowell, T. J., et al. (2008), Impact of terrestrial weather on the upper atmosphere,
675 *Geophys. Res. Lett.*, 35, L09808, *doi:10.1029/2007GL032911*.

676 Garcia, R.R., D.R. Marsh, D.E. Kinnison, B.A. Boville, and F. Sassi (2007), Simulation
677 of secular trends in the middle atmosphere, 1950-2003. *J. Geophys. Res.*, 112, *doi:*
678 *10.1029/2006JD007485*.

679 Gan Q., Du J., Ward W. E., Beagley S. R., Fomichev V. I., Zhang S. (2014) Climatology
680 of the diurnal tides from eCMAM30 (1979 to 2010) and its comparisons with
681 SABER, *Earth Planets Space* 66:103, *doi: 10.1186/1880-5981-66-103*.

682 Hagan, M. E., A. Maute, R. G. Roble, A. D. Richmond, T. J. Immel, and S. L. England
683 (2007), Connections between deep tropical clouds and the Earth's ionosphere,
684 *Geophys. Res. Lett.*, 34, L20109, *doi:10.1029/2007GL030142*.

685 Hagan, M. E., and J. M. Forbes (2002), Migrating and nonmigrating diurnal tides in the
686 middle and upper atmosphere excited by tropospheric latent heat release, *J. Geophys.*
687 *Res.*, 107(D24), 4754, *doi: 10.1029/2001JD001236*.

688 Hagan, M. E., and J. M. Forbes (2003), Migrating and nonmigrating semidiurnal tides in
689 the upper atmosphere excited by tropospheric latent heat release, *J. Geophys. Res.*,
690 108(A2), 1062, *doi:10.1029/2002JA009466*.

691 Heelis, R. A., J. K. Lowell and R. W. Spiro (1982), A model of the high-latitude
692 ionosphere convection pattern, *J. Geophys. Res.*, 87, 6339-6345.

693 Hurrell, J. W., M. M. Holland, P. R. Gent, S. Ghan, J. E. Kay, P. J. Kushner, J.-F.
694 Lamarque, W. G. Large, D. Lawrence, K. Lindsay, W. H. Lipscomb, M. C. Long, N.
695 Mahowald, D. R. Marsh, R. B. Neale, P. Rasch, S. Vavrus, M. Vertenstein, D. Bader,
696 W. D. Collins, J. J. Hack, J. Kiehl, and S. Marshall (2013), The community earth
697 system model: A framework for collaborative research, *Bulletin of the American*
698 *Meteorological Society*, 94, 1339–1360, *doi:10.1175/BAMS-D-12-00121.1*.

699 Immel, T. J., E. Sagawa, S. L. England, S. B. Henderson, M. E. Hagan, S. B. Mende, H.
700 U. Frey, C. M. Swenson, and L. J. Paxton (2006), Control of equatorial

701 ionospheric morphology by atmospheric tides, *Geophys. Res. Lett.*, 33, L15108,
702 doi:10.1029/2006GL026161.

703 Jin, H., Miyoshi, Y., Fujiwara, H., Shinagawa, H. (2008), Electrodynamics of the
704 formation of ionospheric wave number4 longitudinal structure, *Journal of*
705 *Geophysical Research* 113, A09307, <http://dx.doi.org/10.1029/2008JA013301>.

706 Jin, H., Y. Miyoshi, H. Fujiwara, H. Shinagawa, K. Terada, N. Terada, M. Ishii, Y.
707 Otsuka, and A. Saito (2011), Vertical connection from the tropospheric activities to
708 the ionospheric longitudinal structure simulated by a new Earth's whole atmosphere-
709 ionosphere coupled model, *J. Geophys. Res.*, 116, A01316,
710 doi:10.1029/2010JA015925.

711 Jones, M., *Jr.*, J. T. Emmert, D. P. Drob, *and* D. E. Siskind (2017), Middle atmosphere
712 dynamical sources of the semiannual oscillation in the thermosphere and ionosphere,
713 *Geophys. Res. Lett.*, 44, 12–21, doi:10.1002/2016GL071741.

714 Kazimirovsky, E.S., G.V. Vergasova (2009), Mesospheric, lower thermospheric
715 dynamics and external forcing effects: a review. *Indian J. Radio & Space Phys.* 38,
716 7–36.

717 Kil, H., S.-J. Oh, L. J. Paxton, and T.-W. Fang (2009), High-resolution vertical E X B
718 drift model derived from ROCSAT-1data, *J. Geophys. Res.*, 114,
719 A10314,doi:10.1029/2009JA014324.

720 Killeen, T. L., Q. Wu, S. C. Solomon, D. A. Ortland, W. R. Skinner, R. J. Niciejewski,
721 *and* D. A. Gell (2006), TIMED Doppler Interferometer: Overview and recent results,
722 *J. Geophys. Res.*, 111, *A10S01*, doi:10.1029/2005JA011484.

723 Kinnison, D.E., et al. (2007), Sensitivity of chemical tracers to meteorological parameters
724 in the MOZART-3 chemical transport model, *J. Geophys. Res.*, 112, D20302, doi:
725 10.1029/2006JD007879.

726 Kirchoff, V. W. J. H., and B. R. Clemesha (1983), Eddy diffusion coefficients in the
727 lower thermosphere, *J. Geophys. Res.*, 88, 5765–5768.

728 Lastovicka, J. (2006), Forcing of the ionosphere by waves from below, *J. Atmos. Sol.*
729 *Terr. Phys.*, 68, 479–497.

730 Lei, J., et al. (2007), Comparison of COSMIC ionospheric measurements with ground-
731 based observations and model predictions: Preliminary results, *J. Geophys.*
732 *Res.*, 112, A07308, doi:10.1029/2006JA012240.

733 Lieberman R. S., Ortland D. A., Yarosh E. S. (2003), Climatology and interannual
734 variability of diurnal water vapor heating. *J Geophys Res-Atmos* 108(D3): doi:
735 10.1029/2002jd002308.

736 Lieberman R. S., Ortland D. A., Riggin D. M., Wu Q., Jacobi C. (2010), Momentum
737 budget of the migrating diurnal tide in the mesosphere and lower thermosphere. *J*
738 *Geophys Res-Atmos* 115: doi:10.1029/2009jd013684.

739 Lin, C. H., J. Y. Liu, T. W. Fang, P. Y. Chang, H. F. Tsai, C. H. Chen, and C. C. Hsiao
740 (2007), Motions of the equatorial ionization anomaly crests imaged by
741 FORMOSAT-3/COSMIC, *Geophys. Res. Lett.*, 34, L19101,
742 doi:10.1029/2007GL030741.

743 Liu, H.-L. (2016), Variability and predictability of the space environment as related to
744 lower atmosphere forcing, *Space Weather*, 14, doi:10.1002/2016SW001450.

745 Liu, H.-L. et al. (2010), Thermosphere extension of the Whole Atmosphere Community
746 Climate Model, *J. Geophys. Res.*, 115, A12302, doi: 10.1029/2010JA015586.

747 Liu, H.-L., and R. G. Roble (2002), A study of a self-generated stratospheric sudden
748 warming and its mesospheric-lower thermospheric impacts using the coupled TIME-
749 GCM/CCM3, *J. Geophys. Res.*, 107(D23), 4695, doi:10.1029/2001JD001533.

750 Liu, H. -L. and co-authors (2018), Development and Validation of the Whole
751 Atmosphere Community Climate Model with Thermosphere and Ionosphere
752 Extension (WACCM-X), doi: 10.1002/2017MS001232, JAMES.

753 Liu, L., B. Zhao, W. Wan, B. Ning, M. L. Zhang, and M. He (2009), Seasonal variations
754 of the ionospheric electron densities retrieved from Constellation Observing System
755 for Meteorology, Ionosphere, and Climate mission radio occultation measurements,
756 *J. Geophys. Res.*, 114, A02302, doi: 10.1029/2008JA013819.

757 Liu, J., L. Liu, B. Zhao, and W. Wan (2012), Influence of interplanetary solar wind sector
758 polarity on the ionosphere, *J. Geophys. Res.*, 117, A08335, doi:
759 10.1029/2012JA017859.

760 Liu, J., L. Liu, B. Zhao, Y. Wei, L. Hu, and B. Xiong (2012), High-speed stream impacts
761 on the equatorial ionization anomaly region during the deep solar minimum year
762 2008, *J. Geophys. Res.*, 117, A10304, doi:10.1029/2012JA018015.

763 Liu J., Wenbin Wang, Alan Burns, Libo Liu and Joe McNerney (2017), A TIEGCM
764 Numerical Study of the Source and Evolution of Ionospheric F-region Tongues of
765 Ionization: Universal Time and Interplanetary Magnetic Field Dependence, *Journal*
766 *of Atmospheric and Solar-Terrestrial Physics*,
767 <http://dx.doi.org/10.1016/j.jastp.2017.03.005>.

768 Maeda, S., T. J. Fuller-Rowell, and D. S. Evans (1989), Zonally averaged dynamical and
769 compositional response of the thermosphere to auroral activity during September
770 18–24, 1984, *J. Geophys. Res.*, 94, 16,869–16,883.

771 Maute, A., Thermosphere-Ionosphere-Electrodynamics General Circulation Model for
772 the Ionospheric Connection Explorer: TIEGCM-ICON, *Space Sci Rev* (2017).
773 doi:10.1007/s11214-017-0330-3.

774 Marsh, D. R., M.J. Mills, D.E. Kinnison, J.-F. Lamarque, N. Calvo, and L. M. Polvani
775 (2013), Climate change from 1850 to 2005 simulated in CESM1(WACCM), *Journal*
776 *of Climate*, 26, doi:10.1175/JCLI-D-12-00558.1.

777 McLandress C (2002), The seasonal variation of the propagating diurnal tide in the
778 mesosphere and lower thermosphere. Part II: The role of tidal heating and zonal
779 mean winds. *J. Atmos. Sci.* 59(5): 907–922, doi: 10.1175/1520-0469.

780 Mertens, C. J., et al. (2004), SABER observations of mesospheric temperatures and
781 comparisons with falling sphere measurements taken during the 2002 summer
782 MaCWAVE campaign, *Geophys. Res. Lett.*, 31, L0310 5,
783 doi:10.1029/2003GL018605.

784 Miyoshi, Y., and H. Fujiwara (2003), Day-to-day variations of migrating diurnal tide
785 simulated by a GCM from the ground surface to the exobase, *Geophys. Res. Lett.*,
786 30(15), 1789, doi:10.1029/2003GL017695.

787 Millward, G. H., R. J. Moffett, S. Quegan, and T. J. Fuller-Rowell (1996), Ionospheric
788 F2 layer seasonal and semiannual variations, *J. Geophys. Res.*, 101, 5149–5156,
789 doi:10.1029/95JA03343.

790 Oberheide, J., J. M. Forbes, K. Häusler, Q. Wu, and S. L. Bruinsma (2009), Tropospheric
791 tides from 80 to 400 km: Propagation, interannual variability, and solar cycle effects,
792 *J. Geophys. Res.*, 114, D00I05, doi:10.1029/2009JD012388.

793 Pedatella, N. M., K. Raeder, J. L. Anderson, and H. -L. Liu (2013), Application of data
794 assimilation in the Whole Atmosphere Community Climate Model to the study of
795 day-to-day variability in the middle and upper atmosphere, *Geophys. Res. Lett.*, 40,
796 4469–4474, doi:10.1002/grl.50884.

797 Qian, L., S. C. Solomon, and T. J. Kane (2009), Seasonal variation of thermospheric
798 density and composition, *J. Geophys. Res.*, 114, A01312,
799 doi:10.1029/2008JA013643.

800 Qian, L., A. G. Burns, S. C. Solomon, and W. Wang (2013), Annual/semiannual variation
801 of the ionosphere, *Geophys. Res. Lett.*, 40,1928–1933, doi:10.1002/grl.50448.

802 Qian, L., A. G. Burns, B. A. Emery, B. Foster, G. Lu, A. Maute, A. D. Richmond, R. G.
803 Roble, S. C. Solomon, and W. Wang (2014), The NCAR TIE-GCM: A community
804 model of the coupled thermosphere/ionosphere system, in *Modeling the Ionosphere-*
805 *Thermosphere System*, J. Huba, R. Schunk, and G. Khazanov, eds., *AGU*
806 *Geophysical Monograph Series*, 201, 73, doi:10.1002/9781118704417.ch7.

807 Qian, L., and J. Yue (2017), Impact of the lower thermospheric winter-to-summer
808 residual circulation on thermospheric composition, *Geophys. Res. Lett.*, 44,
809 doi:10.1002/2017GL073361.

810 Ren, Z., Wan, W., Xiong, J., Liu, L. (2010), Simulated wave number 4 structure in
811 equatorial F-region vertical plasma drifts. *Journal of Geophysical Research* 115,
812 A05301, <http://dx.doi.org/10.1029/2009JA014746>.

813 Remsberg, E. E., et al. (2008), Assessment of the quality of the Version 1.07
814 temperature-versus-pressure profiles of the middle atmosphere from
815 TIMED/SABER, *J. Geophys. Res.*, 113, D17101, doi: 10.1029/2008JD010013.

816 Richter, J.H., F. Sassi and R.R. Garcia (2010). Toward a physically based gravity wave
817 source parameterization in a General Circulation Model., *J. Atmos. Sci.*, 67 (1), 136-
818 156, doi:10.1175/2009JAS3112.1.

819 Rienecker et al. (2011), MERRA: NASA’s Modern-Era Retrospective Analysis for
820 Research and Applications, *J. Climate*, 24, 3624-3648, doi:10.1175/JCLI-D-11-
821 00015.1

822 Rishbeth, H. (1998), How the thermospheric circulation affects the ionospheric F2-layer,
823 *J. Atmos. Sol. Terr. Phys.*, 60, 1385–1402.

824 Rishbeth, H. (2000), The equatorial *F*-layer: Progress and puzzles, *Ann. Geophys.*, 18,
825 730.

826 Roble, R. G., R. E. Dickinson, and E. C. Ridley (1982), Global circulation and
827 temperature structure of thermosphere with high-latitude plasma convection, *J.*
828 *Geophys. Res.*, 87, 1599–1614.

829 Roble, R. G., and E. C. Ridley (1987), An auroral model for the NCAR thermosphere
830 general circulation model (TGCM), *Ann. Geophys.*, 5A, 369-382.

831 Roble, R. G., and E. C. Ridley (1994), A thermosphere-ionosphere- mesosphere-
832 electrodynamics general circulation model (time-GCM), *Geophys. Res. Lett.*, 21,
833 417–420.

834 Roble, R.G. (2000), On the Feasibility of Developing a Global Atmospheric Model
835 Extending from the Ground to the Exosphere, in *Atmospheric Science Across the*
836 *Stratopause* (eds D. E. Siskind, S. D. Eckermann and M. E. Summers), American
837 Geophysical Union, Washington, D. C.. doi: 10.1029/GM123p0053.

838 Sasi, M. N., and L. Vijayan (2001), Turbulence characteristics in the tropical mesosphere

839 as obtained by MST radar at Gadanki (13.5°N, 79.2°E), *Ann. Geophys.*, 19, 1019–
840 1025.

841 Sagawa, E., Immel, T.J., Frey, H.U., Mende, S.B. (2005), Longitudinal structure of the
842 equatorial anomaly in the nighttime ionosphere observed by IMAGE/FUV, *Journal*
843 *of Geophysical Research* 110, A11302, <http://dx.doi.org/10.1029/2004JA010848>.

844 Scherliess, L., and B. G. Fejer (1999), Radar and satellite global equatorial F region
845 vertical drift model, *J. Geophys. Res.*, 104(A4), 6829-6842, doi:
846 10.1029/1999JA900025.

847 Schreiner, W. S., S. V. Sokolovskiy, C. Rocken, and D. C. Hunt, (1999), Analysis and
848 validation of GPS/MET radio occultation data in the ionosphere. *Radio Sci.*, 34(4),
849 949-966, doi: 10.1029/1999RS900034.

850 Solomon, S. C., L. Qian, and A. G. Burns (2013), The anomalous ionosphere between
851 solar cycles 23 and 24, *J. Geophys. Res. Space Physics*, 118, 6524,
852 doi:10.1002/jgra.50561.

853 Stoneback, R. A., R. A. Heelis, A. G. Burrell, W. R. Coley, B. G. Fejer, and E. Pacheco
854 (2011), Observations of quiet time vertical ion drift in the equatorial ionosphere
855 during the solar minimum period of 2009, *J. Geophys. Res.*, 116, A12327, doi:
856 10.1029/2011JA016712.

857 Strom, S. R. and G. Iwanaga (2005), Overview and History of the Defense
858 Meteorological Satellite Program, Crosslink, The Aerospace Corporation magazine
859 of advances in aerospace technology, Vol. 6, No 1.

860 Su, S.-Y., C. K. Chao, and C. H. Liu (2008), On monthly/seasonal/longitudinal variations
861 of equatorial irregularity occurrences and their relationship with the postsunset
862 vertical drift velocities, *J. Geophys. Res.*, 113, A05307, doi:10.1029/2007JA012809.

863 Sutton, E. K., J. P. Thayer, W. Wang, S. C. Solomon, X. Liu, and B. T. Foster (2015), A
864 self-consistent model of helium in the thermosphere, *J. Geophys. Res. Space Physics*,
865 120, 6884–6900, doi:10.1002/2015JA021223.

866 Wan, W., Z. Ren, F. Ding, J. Xiong, L. Liu, B. Ning, B. Zhao, G. Li, and M. -L. Zhang
867 (2012), A simulation study for the couplings between DE3 tide and longitudinal
868 WN4 structure in the thermosphere and ionosphere, *J. Atmos. Sol. Terr. Phys.*, 90-
869 91, 52–60, doi: 10.1016/j.jastp.2012.04.011.

870 Wu, Q., D. A. Ortland, T. L. Killeen, R. G. Roble, M. E. Hagan, H.-L. Liu, S. C.
871 Solomon, J. Xu, W. R. Skinner, and R. J. Niciejewski (2008), Global distribution
872 and interannual variations of mesospheric and lower thermospheric neutral wind
873 diurnal tide:1. Migrating tide, *J. Geophys. Res.*, 113, A05308, doi:
874 10.1029/2007JA012542.

875 Wu, Q., D. A. Ortland, B. Foster, and R. G. Roble (2012), Simulation of nonmigrating
876 tide influences on the thermosphere and ionosphere with a TIMED data driven
877 TIEGCM, *J. Atmos. Sol. Terr. Phys.*, 90-91, 61–67, doi: 10.1016/j.jastp.2012.02.009.

878 Xu J. Y., Smith AK, Liu HL, Yuan W, Wu Q, Jiang GY, Mlynczak MG, Russell JM,
879 Franke SJ (2009), Seasonal and quasi-biennial variations in the migrating diurnal
880 tide observed by Thermosphere, Ionosphere, Mesosphere, Energetics and Dynamics
881 (TIMED). *J Geophys Res-Atmos* 114: doi: 10.1029/2008jd011298.

882 Yamazaki, Y., and A. D. Richmond (2013), A theory of ionospheric response to upward-
883 propagating tides: Electrodynamical effects and tidal mixing effects, *J. Geophys. Res.*
884 *Space Physics*, 118, 5891–5905, doi: 10.1002/jgra.50487.

885 Yue, J., and W. Wang (2014), Changes of thermospheric composition and ionospheric
886 density caused by quasi two-day wave dissipation, *J. Geophys. Res. Space Physics*,
887 119, 2069–2078, doi:10.1002/2013JA019725.

888 Yue, X., W. S. Schreiner, J. Lei, S. V. Sokolovskiy, C. Rocken, D. C. Hunt, and Y.-H.
889 Kuo (2010), Error analysis of Abel retrieved electron density profiles from radio-
890 occultation measurements, *Ann. Geophys.*, 28, 217–222.

891 Zhang, S.-R., Z. Chen, A. J. Coster, P. J. Erickson, and J. C. Foster (2013), Ionospheric
892 symmetry caused by geomagnetic declination over North America, *Geophys. Res.*
893 *Lett.*, 40, 1-5, doi:10.1002/2013GL057933.

894 Zhang X. L., Forbes JM, Hagan ME, Russell JM, Palo SE, Mertens CJ, Mlynczak MG
895 (2006), Monthly tidal temperatures 20–120 km from TIMED/SABER. *J Geophys*
896 *Res* 111(A10): doi: 10.1029/2005ja011504.

897
898
899
900
901
902
903
904
905
906
907
908
909
910
911
912
913
914
915
916
917
918
919
920
921
922
923
924
925
926
927
928
929
930

931 **Figures**

932 Figure 1. Comparisons of hmF₂ (in units of km) between WACCM-X, COSMIC, and
933 TIE-GCM at March Equinox.

934 Figure 2. The same as Figure 1 but at June Solstice.

935 Figure 3. Comparisons of NmF₂ (in units of m⁻³) between WACCM-X, COSMIC, and
936 TIE-GCM at March Equinox.

937 Figure 4. The same as Figure 3 but at June Solstice.

938 Figure 5. (a) Ionosphere NmF₂ (in units of m⁻³) and (c) hmF₂ (in units of km) measured
939 by the ionosonde at Jicamarca (12°S, 283°W, 1°N geomagnetic latitude) during
940 days 300-320 in 2008. Scatter plots between observations (black line) and
941 WACCM-X (red line) of (b) NmF₂ and (d) hmF₂ during days 60-366 in 2008.
942 The correlation coefficients are given in Figures 5b and 5d.

943 Figure 6. The same as Figure 5, but for Boulder (40.0° N, 254.7° W, 48.9° geomagnetic
944 latitude).

945 Figure 7. Comparisons of vertical ion drifts (in units of m/s) over Jicamarca (12° S, 76.8°
946 W) between WACCM-X (red solid line), TIE-GCM (red dashed line), Fejer-
947 Scherliess empirical model (blue line), and C/NOFS observations (black cross).

948 Figure 8. Latitude-altitude cross-sections of temperature amplitude (in Kelvin) and zonal
949 wind amplitude (in m/s) of DW1 in March from WACCM-X (left panels),
950 SABER (right left) and TIDI (bottom right) observations.

951 Figure 9. The same as Figure 8 but for SW2.

952 Figure 10. The same as Figure 8 but for DE3.

953 Figure 11. Seasonal variations of temperature amplitude (in Kelvin) of DW1 at 95 km,
954 DE3 at 110 km, and SW2 at 105 km from WACCM-X (left panel) and SABER
955 observations (right panel).

956 Figure 12. Seasonal variations of climatological NmF₂, hmF₂, vertical drift (m/s), O/N₂,
957 meridional wind (m/s), eddy diffusion coefficient (K_{zz}) from WACCM-X (left
958 panel) and SABER observations (right panel) on the dayside (09-15 LT). Vertical
959 Drift, O/N₂, Meridional wind are shown at 300 km, while K_{zz} is shown at 110 km.

Figure1.

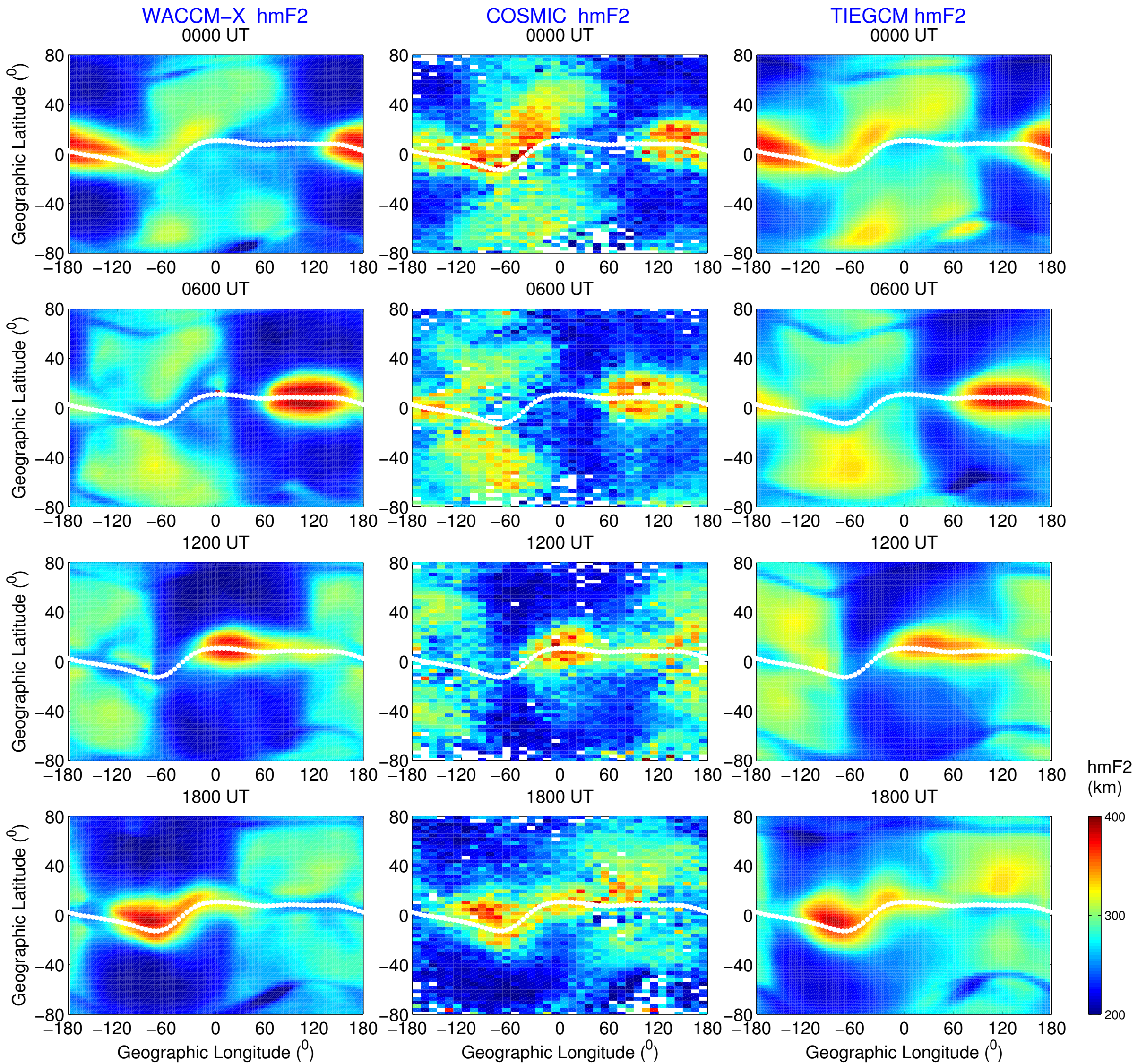


Figure2.

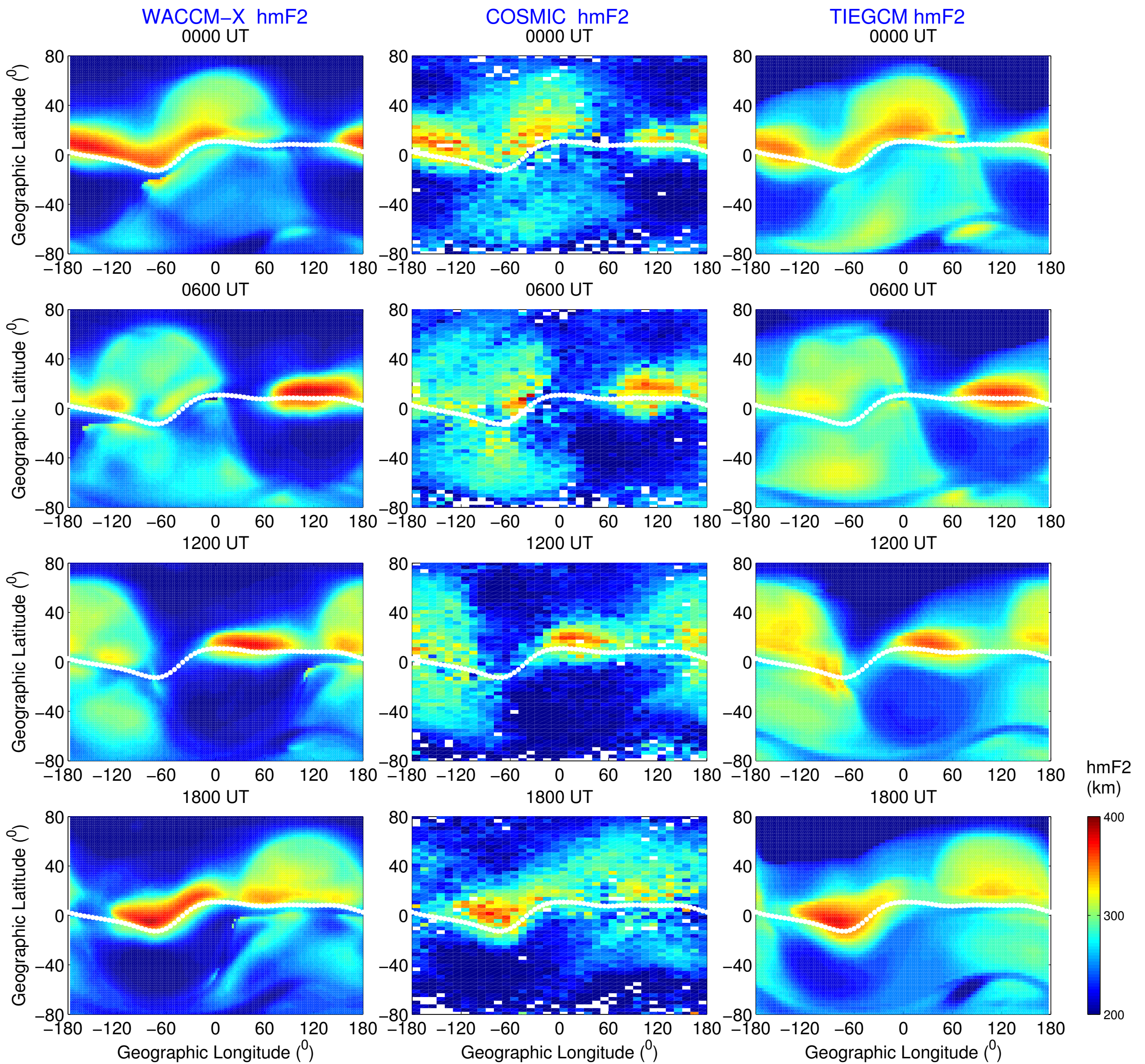


Figure3.

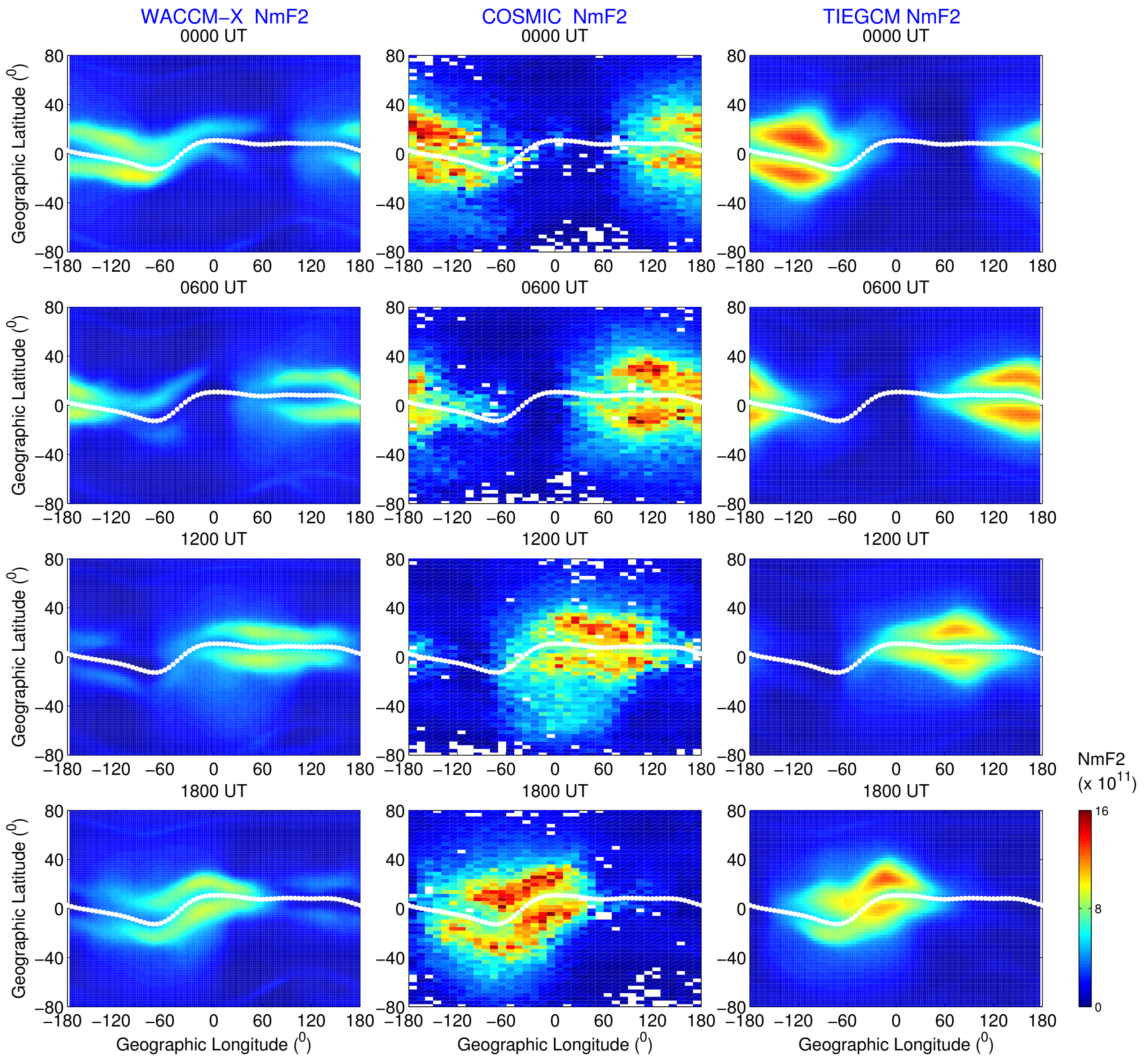


Figure4.

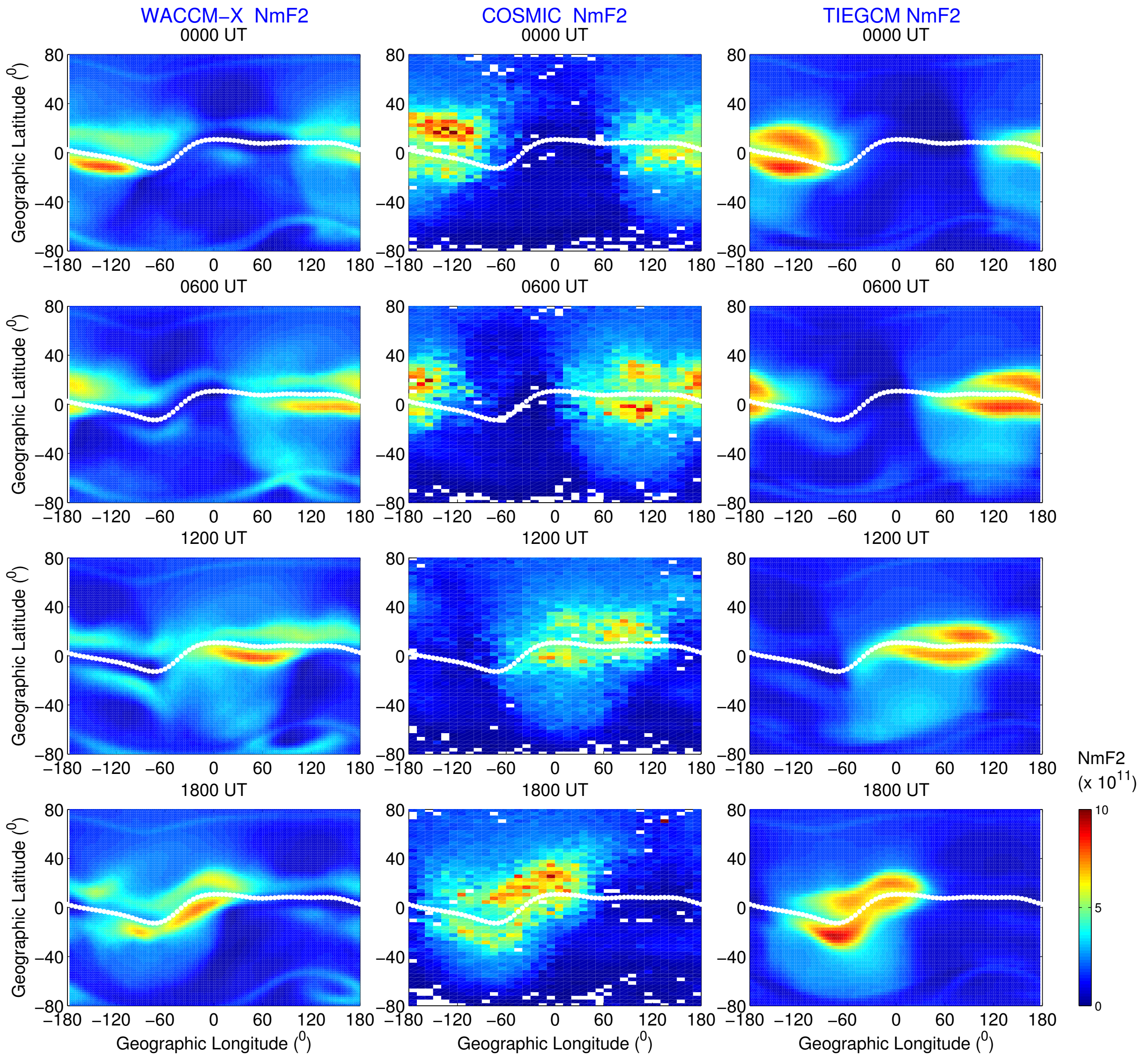


Figure 5.

Jicamarca (12° S, 76.8° W)

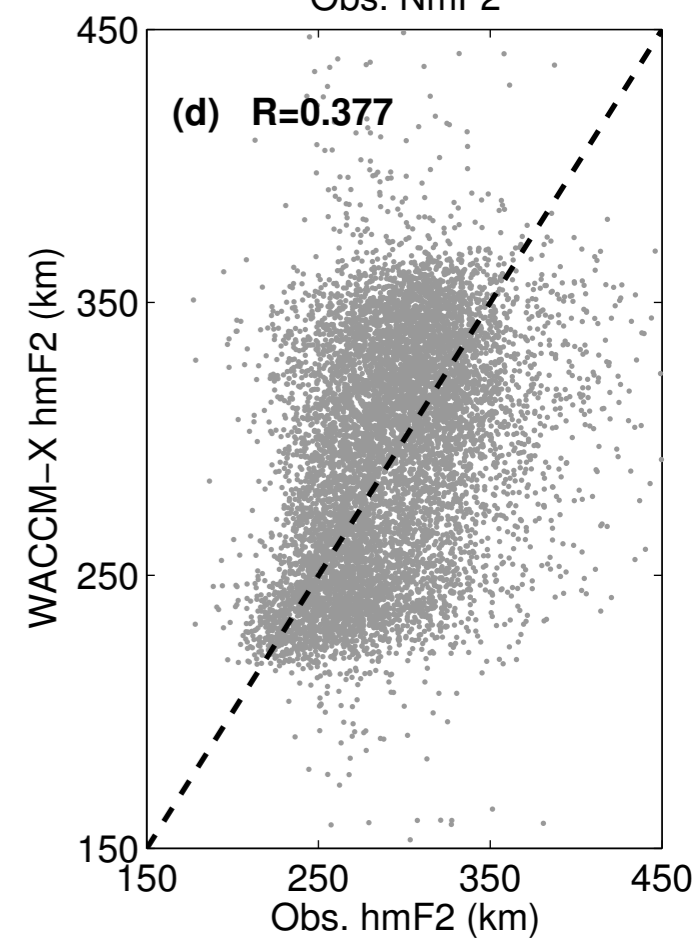
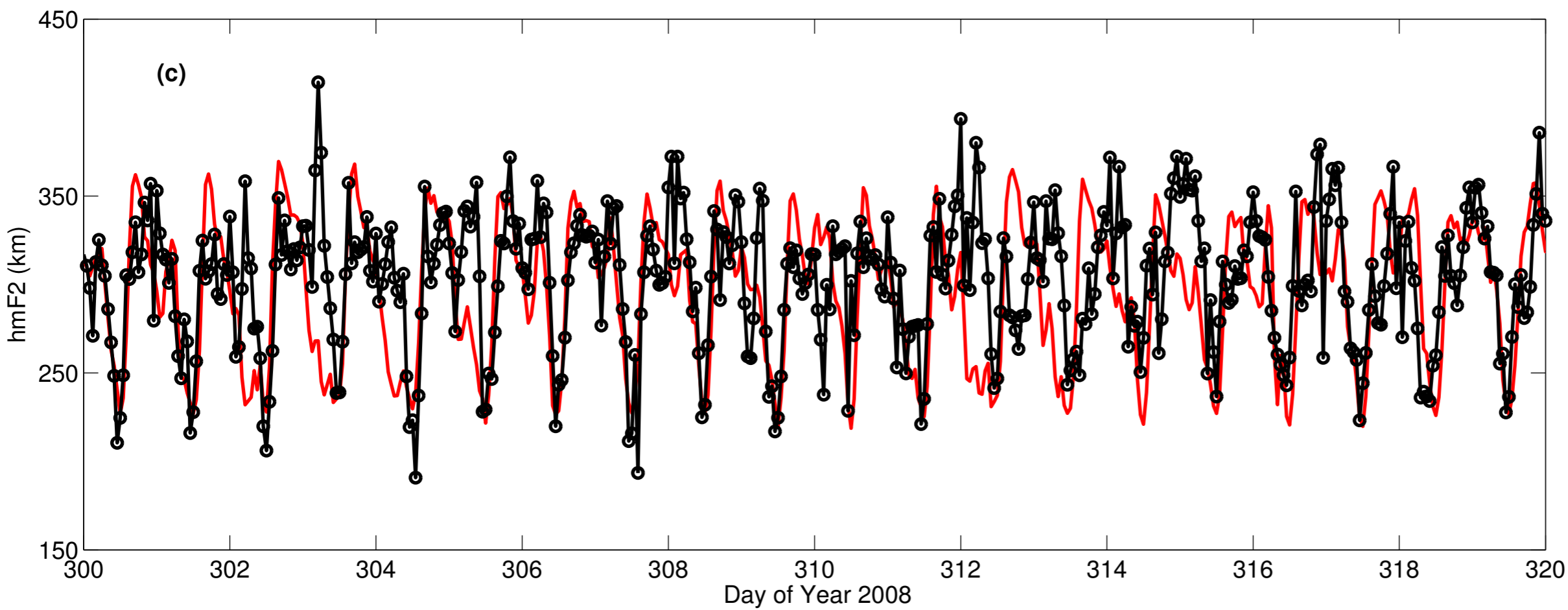
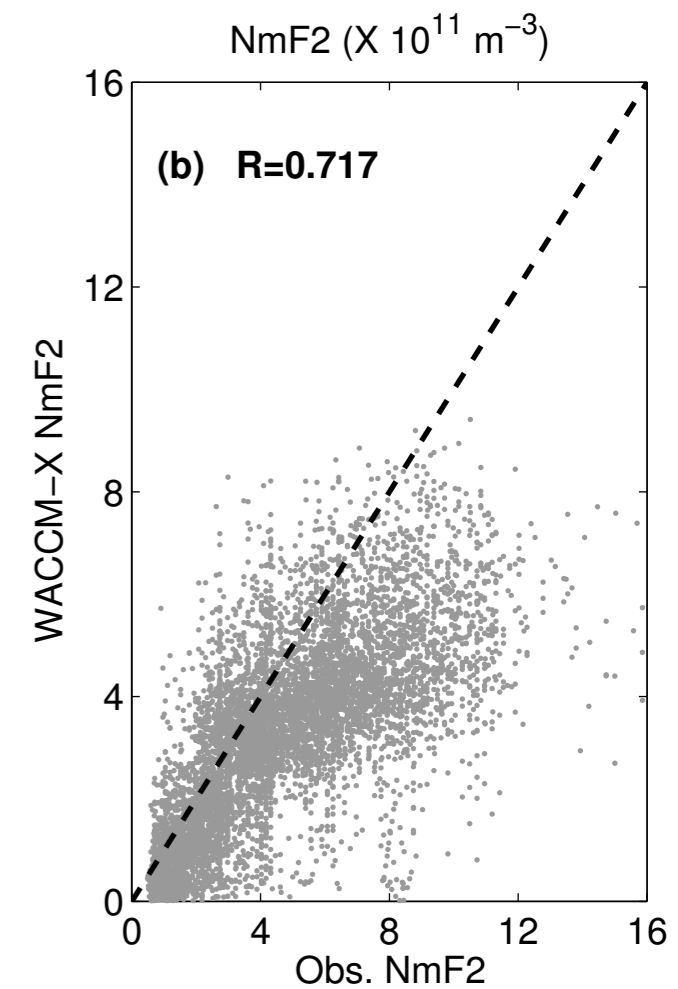
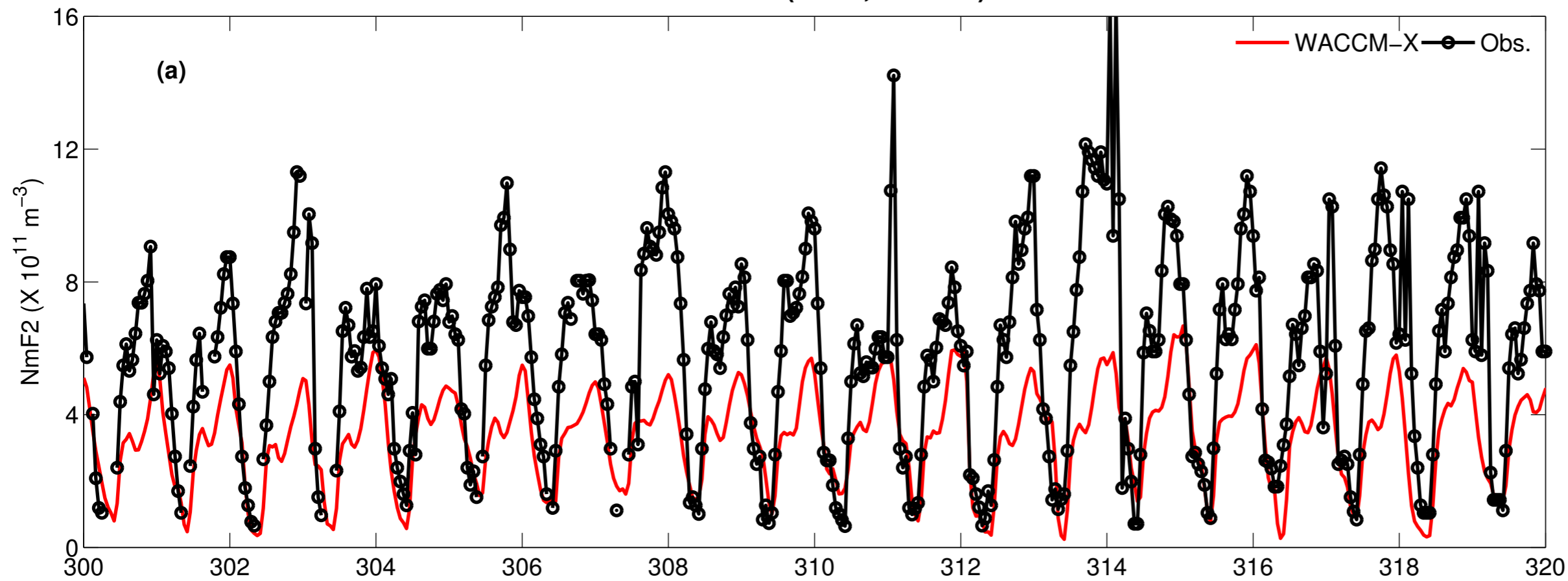


Figure 6.

Boulder (40.0° N, 105° W)

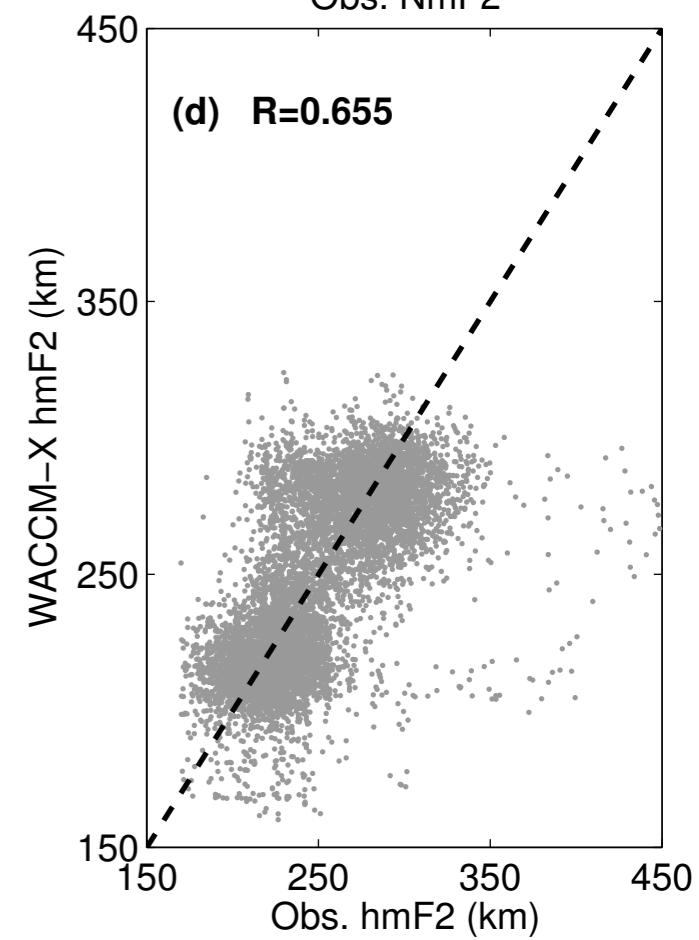
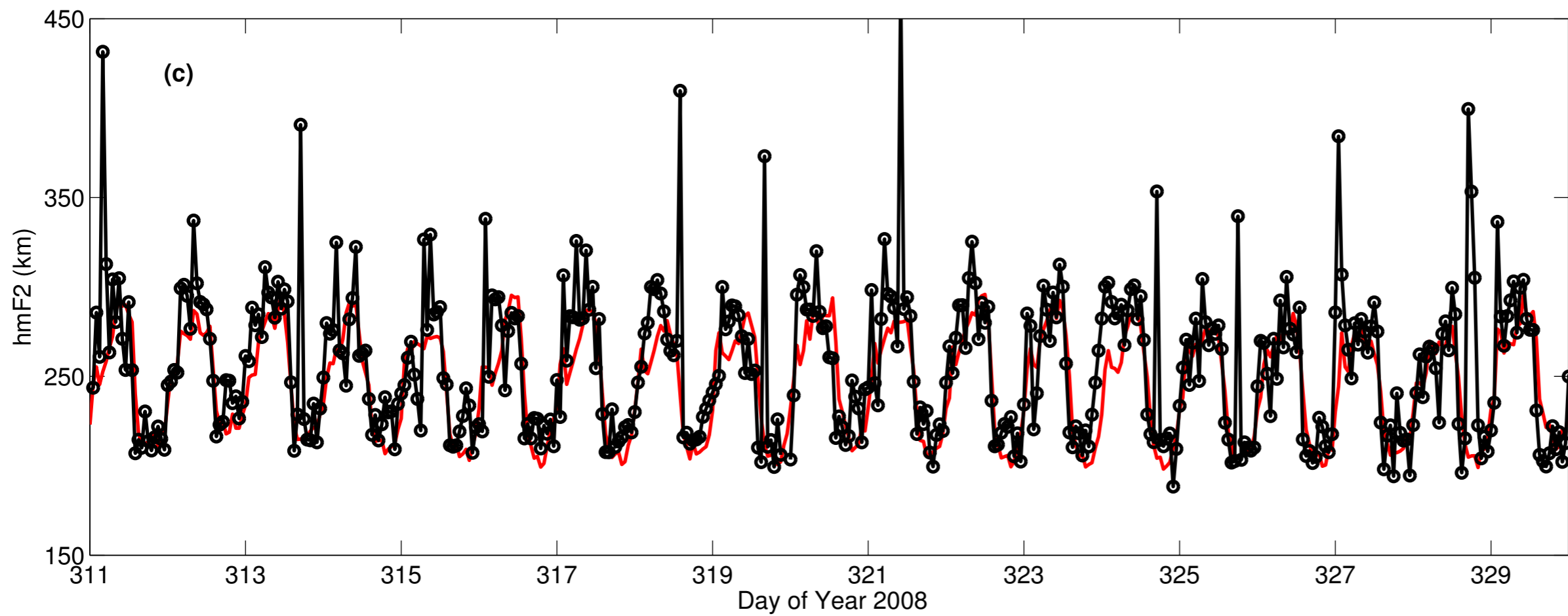
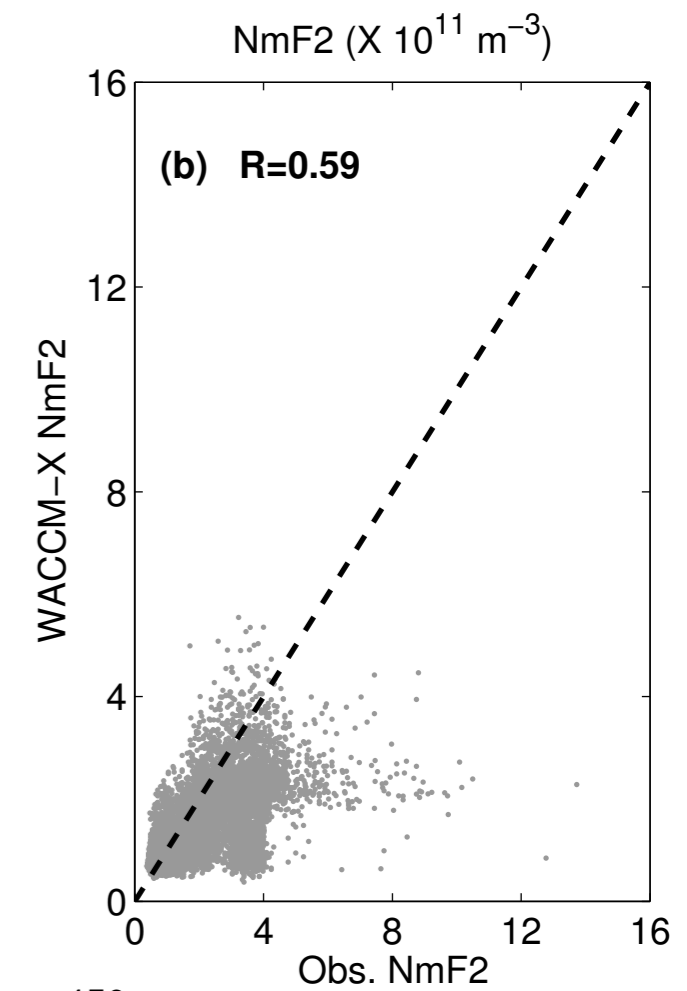
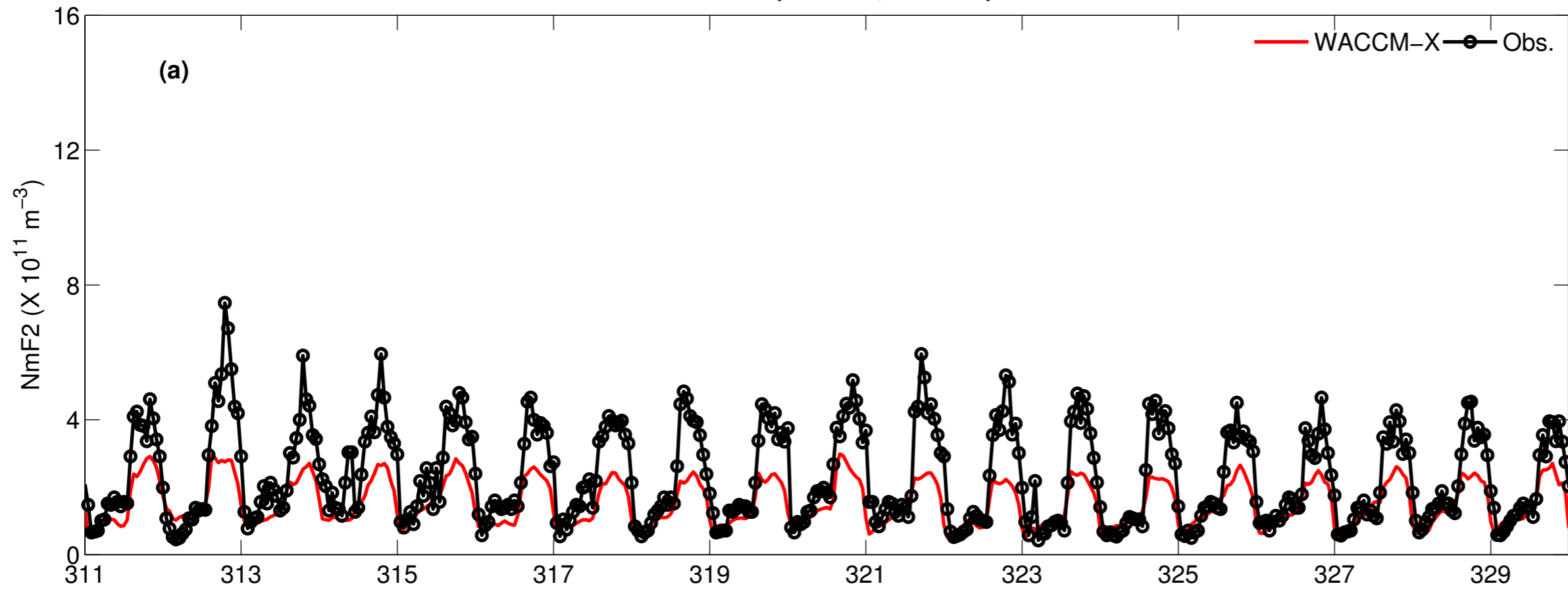
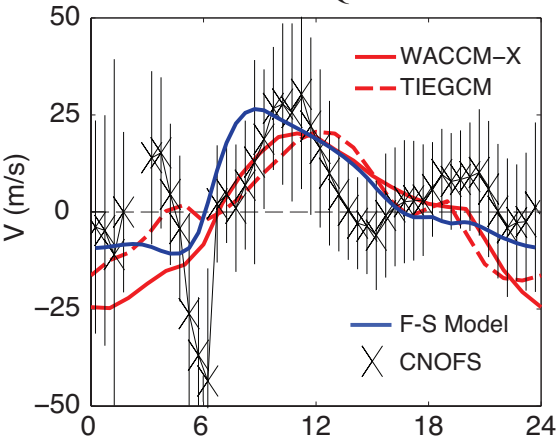
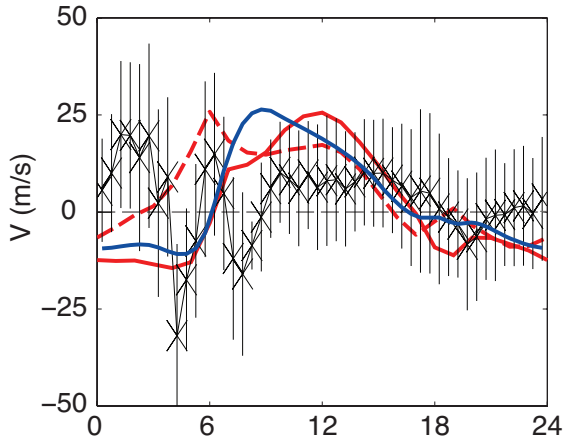


Figure 7.

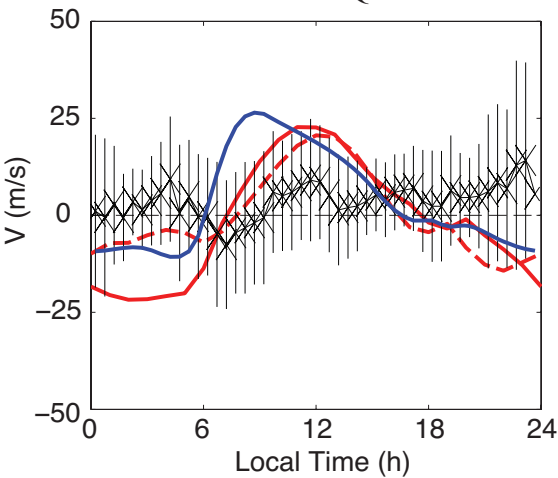
MARCH EQUINOX



JUNE SOLSTICE



SEPTEMBER EQUINOX



DECEMBER SOLSTICE

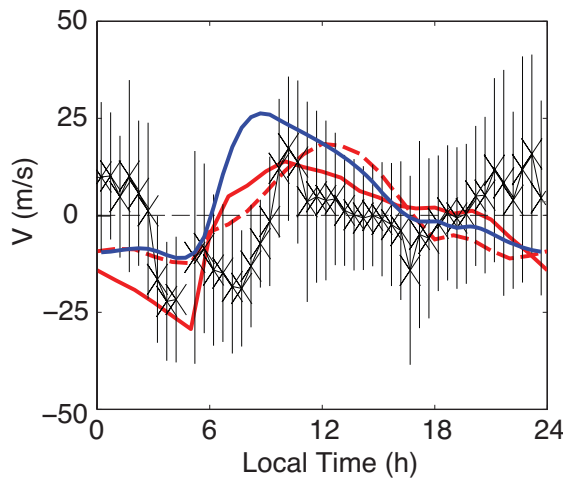
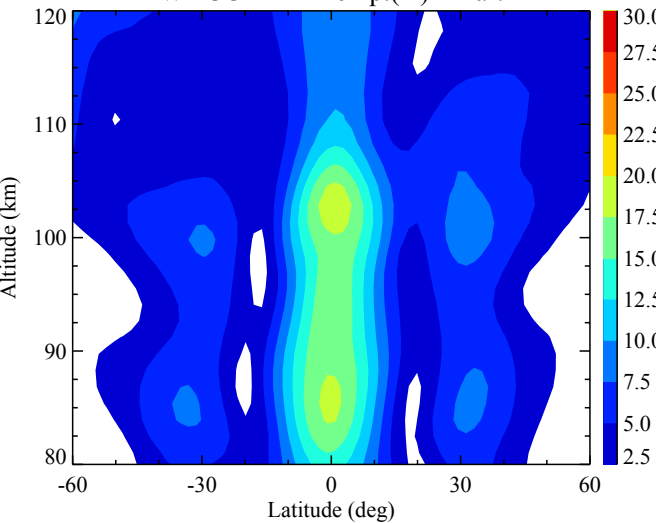
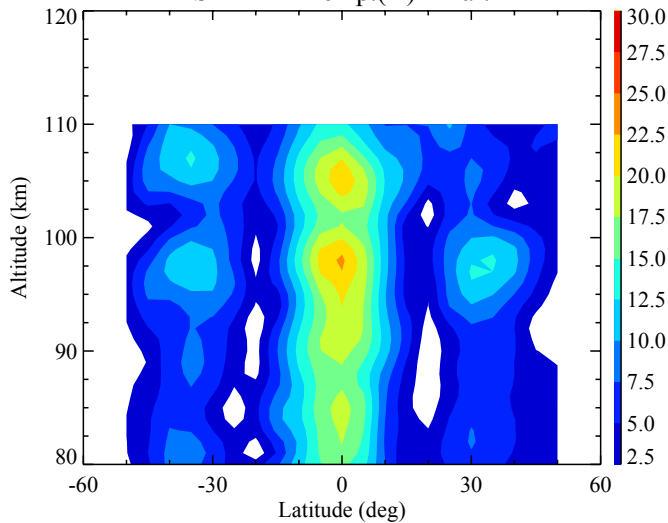


Figure8.

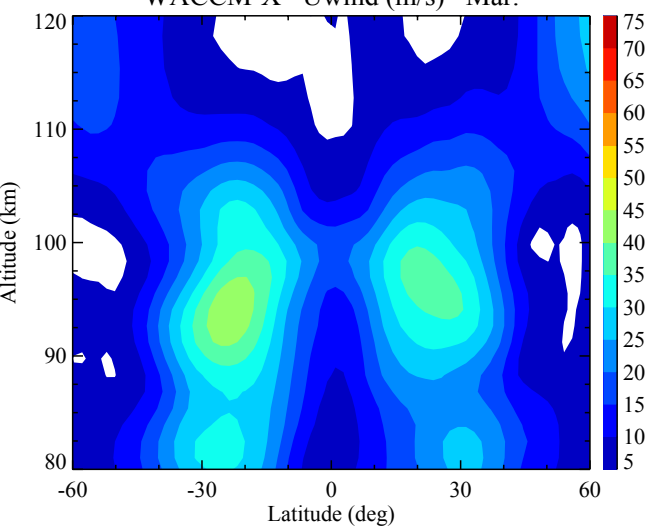
WACCM-X Temp.(K) Mar.



SABER Temp.(K) Mar.



WACCM-X Uwind (m/s) Mar.



TIDI Uwind (m/s) Mar.

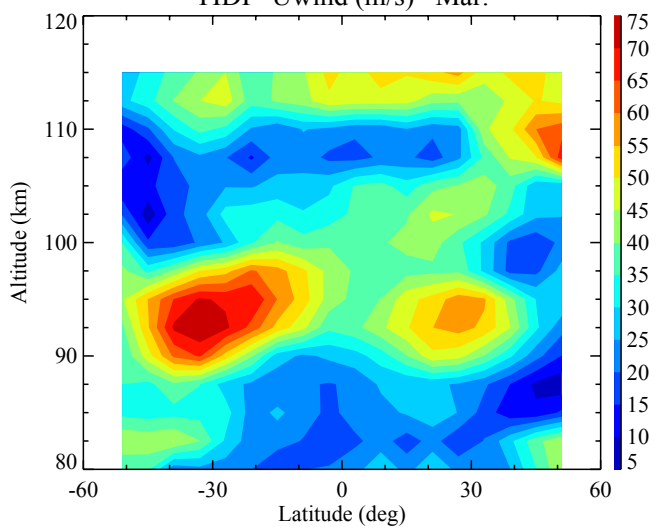
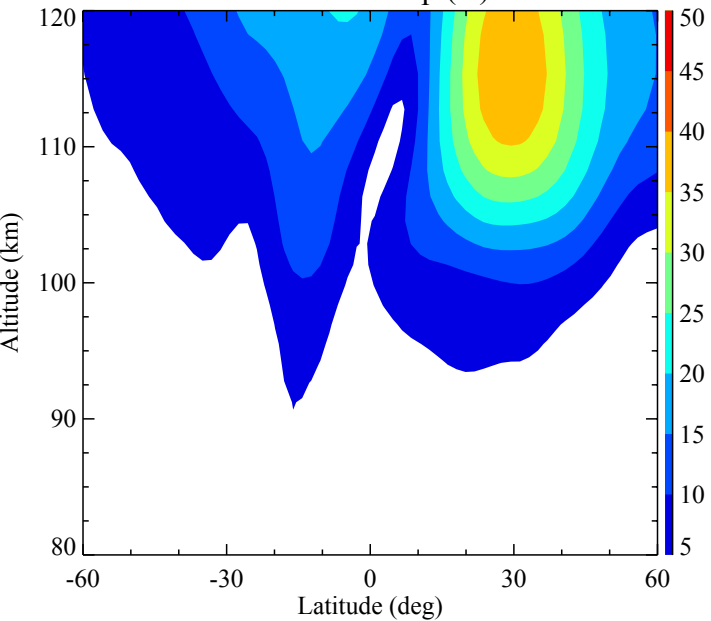
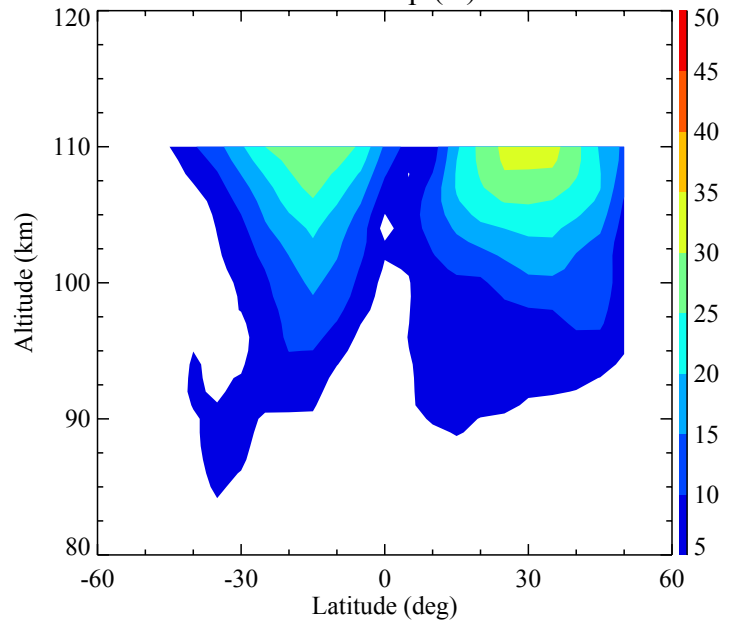


Figure9.

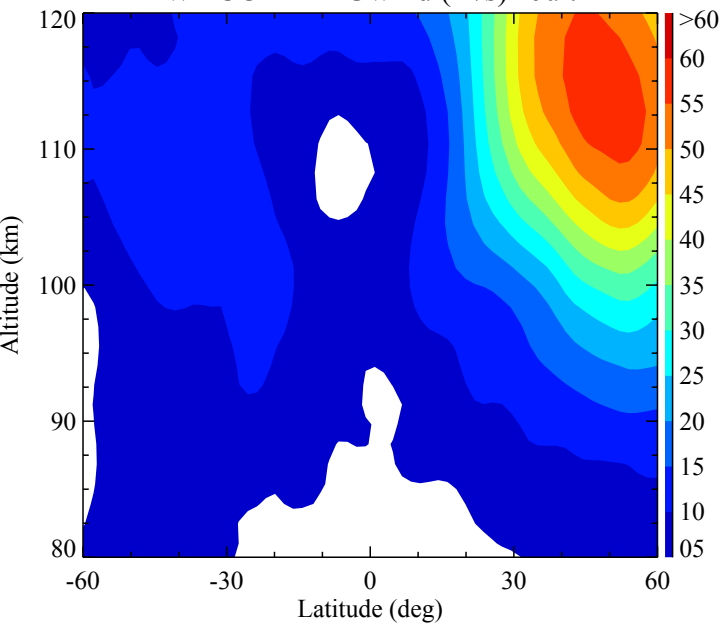
WACCM-X Temp.(K) Jul.



SABER Temp.(K) Jul.



WACCM-X Uwind (m/s) Jul.



TIDI Uwind (m/s) Jul.

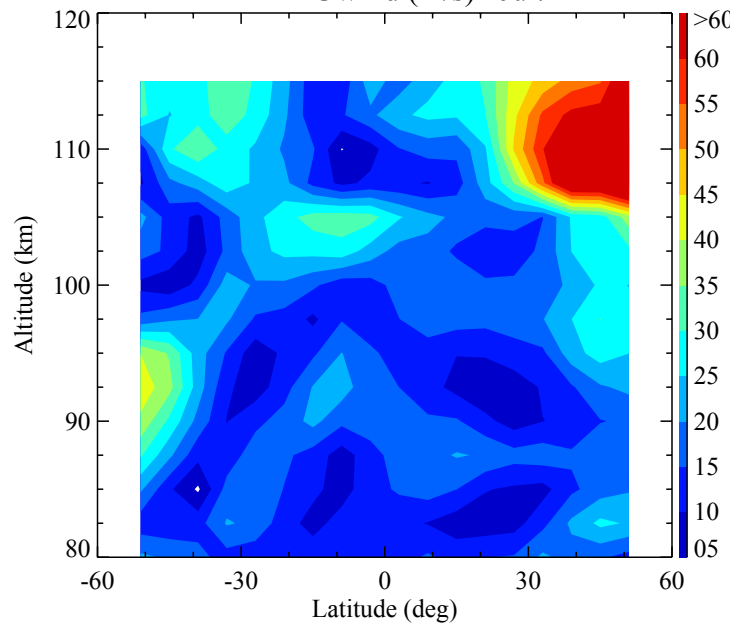
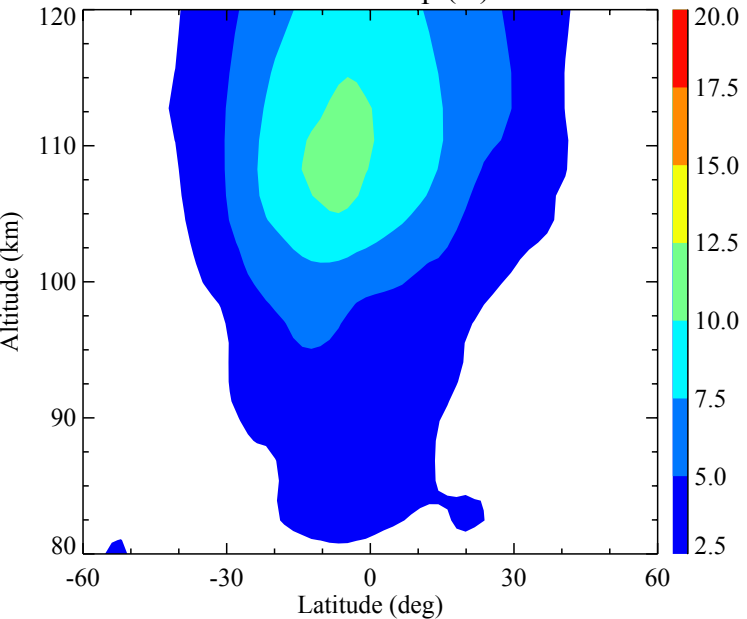
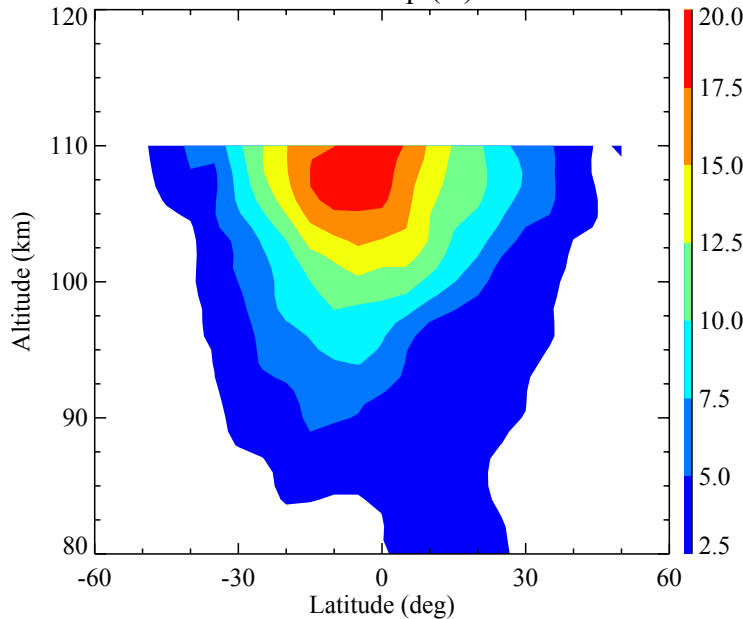


Figure10.

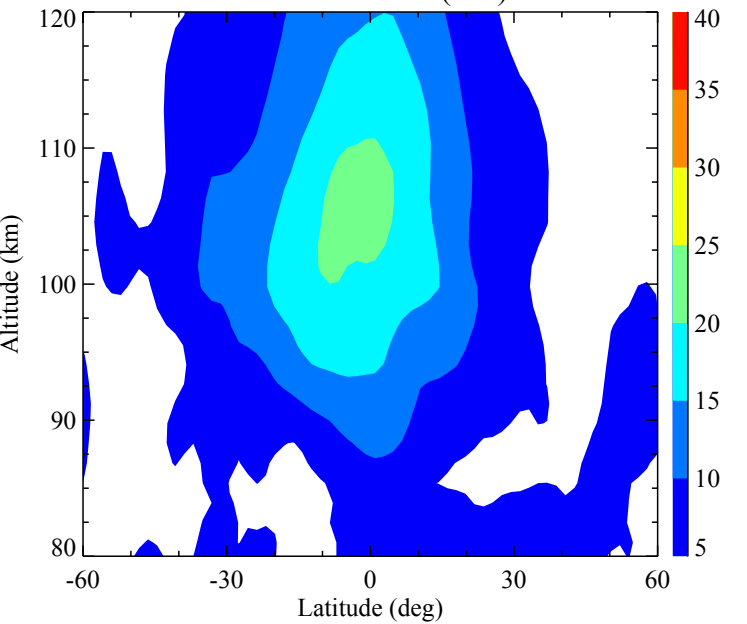
WACCM-X Temp.(K) Jul.



SABER Temp.(K) Jul.



WACCM-X Uwind (m/s) Jul.



TIDI Uwind (m/s) Jul.

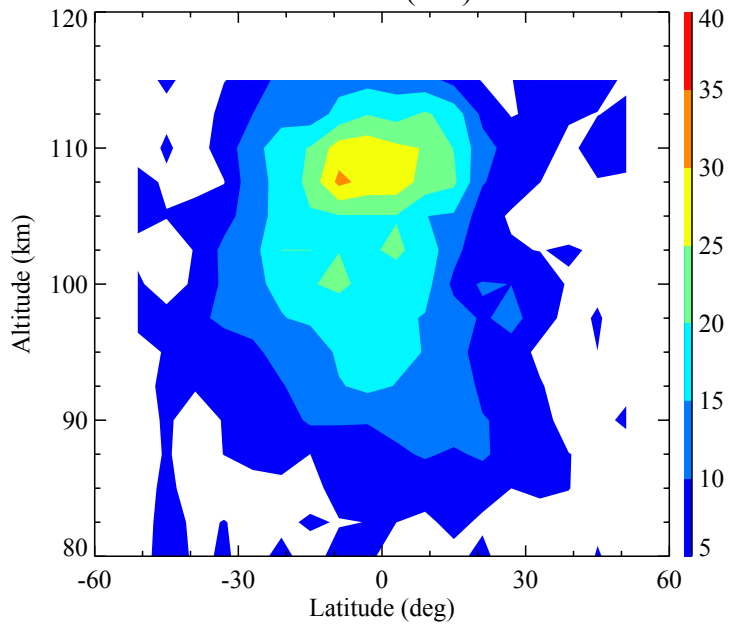
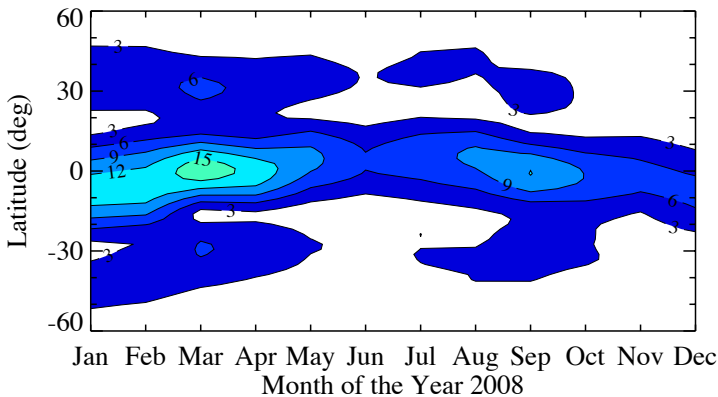
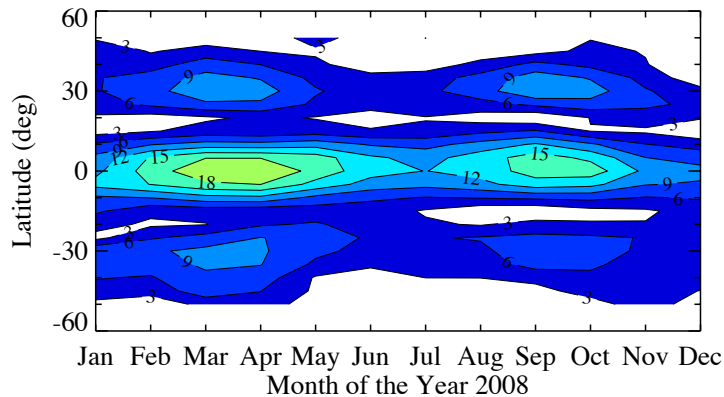


Figure11.

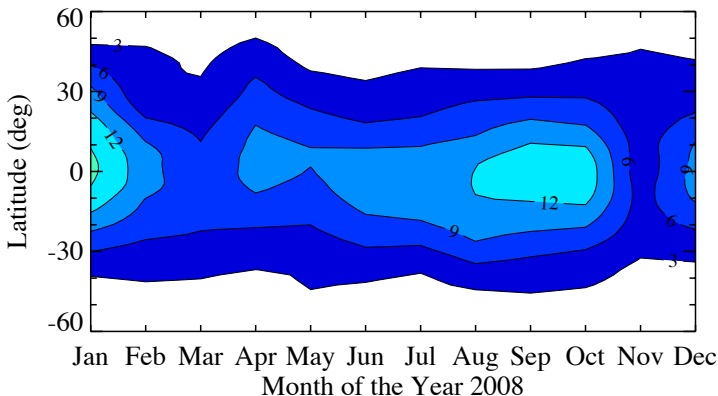
WACCM-X Alt = 95 km DW1



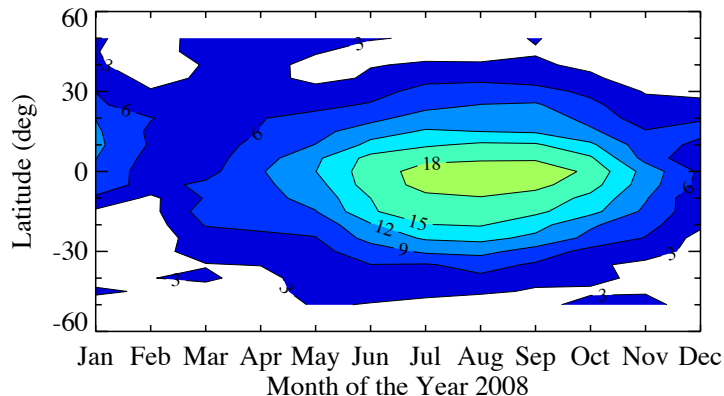
SABER Alt = 95 km DW1



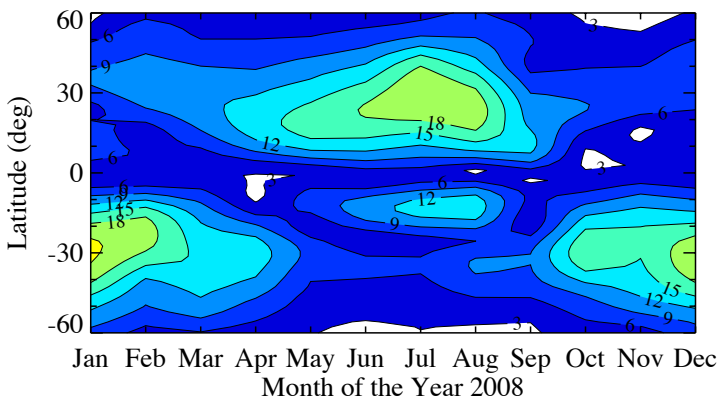
WACCM-X Alt = 110 km DE3



SABER Alt = 110 km DE3



WACCM-X Alt = 105 km SW2



SABER Alt = 105 km SW2

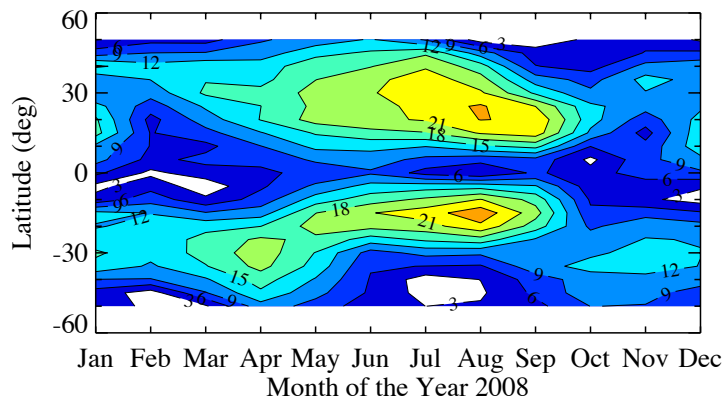


Figure12.

